Opening of the Algerian Basin: Petrological, geochemical and geochronological constraints from the Yaddene Complex (Lesser Kabylia, Northeastern Algeria)

Abderraouf Seffari, Nachida Abdallah, Olivier Bruguier, Delphine Bosch, Abdehafid Afalfiz, Abdelkrim Yelles-Chaouche, Abdelmalek Lekoui, Aziouz Ouabadi

Opening of the Algerian Basin: Petrological, geochemical and geochronological constraints from the Yaddene Complex (Lesser Kabylia, Northeastern Algeria)

Abderraouf Seffari [a,b,*], Nachida Abdallah [a], Olivier Bruguier [c], Delphine Bosch [c], Abdehafid Afalfiz [a], AbdelKrim Yelles-Chaouche [b], Abdelmalek Lekoui [d], Aziouz Ouabadi [a]

[a] Laboratoire de Géodynamique Géologie de l'Ingénieur et Planétologie, Faculty of Earth Sciences, Geography and Country Planning FSTAGT/USTHB, Algeria
[b] Center of Research in Astronomy, Astrophysics, and Geophysics (C.R.A.A.G.), BP 63, 16340, Bouzaréah, Algiers, Algeria
[c] Géosciences Montpellier, CNRS - Université de Montpellier, Place E. Bataillon, 34 095, Montpellier, France
[d] Laboratoire de génie géologique, Département des Sciences de la Terre et de l'Univers, Université Mohamed Seddik Ben Yahia, Jijel, Algeria

ARTICLE INFO

Keywords:
Western Mediterranean
Algerian basin
Rifting
Mafic/ultramafic layered complex
Thermobarometry
U/Pb geochronology.

ABSTRACT

The Yaddene complex, located in Lesser Kabylia (northeastern Algeria), is composed of Tertiary mafic and ultramafic rocks that outcrop within syn-rift sedimentary rocks of the Algerian marginal basin, in the Maghrebide belt of North Africa. Petrographic observations show that the Yaddene complex is composed mainly of two distinct lithologies: (1) a layered quartz-bearing gabbro at the bottom, which consists mainly of plagioclase (An_{93}), clinopyroxene (altered to actinolite) and rare interstitial quartz; and (2) layered plagioclase-bearing lherzolites composed of olivine ($Fo_{86\text{-}88}$) orthopyroxene (En_{86-87}), clinopyroxene (diopside and augite), rare plagioclase (anorthite) and amphibole of pargasitic composition.

The trace element concentrations in pyroxenes and olivine of the Yadenne complex show a depletion in light rare earth elements (LREE) similar to basalts of the Mid-Ocean Ridge (N-MORB), which reflects the depletion of the mantle source. In addition, high #Cr in spinel reflects a high degree of partial melting of the mantle source. On the other hand, slight enrichment in Large Ion Lithophile Elements (Cs, Rb, Ba), weak but significant negative Nb, Ta, Zr, Hf and Ti anomalies, and positive Pb spikes are observed in both whole-rocks and minerals. These patterns are best explained by interaction between parental mantle and fluids and/or siliceous melts derived from a subducting oceanic slab. The tectonic discrimination diagrams of minerals and whole rocks indicate that the most likely geodynamic setting for emplacement of the Yaddene Complex is a back arc basin environment.

In situ U-Pb dating of euhedral zircons and titanite from a quartz-bearing gabbro yields an age of 18.97 ± 0.12 Ma (2σ), which is interpreted as the crystallization age of magmatic zircons and the gabbroic magma. Zircons from a plagioclase-bearing lherzolite gave a consistent age of 19.05 ± 0.39 Ma (2σ), which is attributed to zircon growth during metamorphic/metasomatic processes coeval to gabbroic magma emplacement. The mafic/ultramafic rocks of the Yaddene complex are intercalated within fine-grained sediments of the syn-rift "Oligo-Miocene Kabyle" and the obtained early Burdigalian ages are interpreted as the early stages of an extensional regime that ultimately led to the opening of the oceanic Algerian Basin.

1. Introduction

The western Mediterranean formed from the interplay of different continental and oceanic lithospheric plates that shaped this area since the breakup of Pangea and the Mesozoic opening of the Tethys Ocean and subordinate oceanic basins, such as the Ligurian Ocean (Michard et al., 2006; van Hinsbergen et al., 2004; Leprêtre et al., 2018; Romagny et al., 2020). It is believed that the Western Mediterranean evolved during the Cenozoic mainly by retreat of the Tethyan slab and back-arc extension that migrated broadly southeastward (Liguro-Provençal basin and Tyrrhenian Sea) or southwestward (Alboran area). Simultaneously, some domains experienced strong back-arc extension and emplacement

* Corresponding author. Laboratoire de Géodynamique Géologie de l'Ingénieur et Planétologie, Faculty of Earth Sciences, Geography and Country Planning FSTAGT/USTHB, Algeria.
E-mail address: seffari.abdr@gmail.com (A. Seffari).

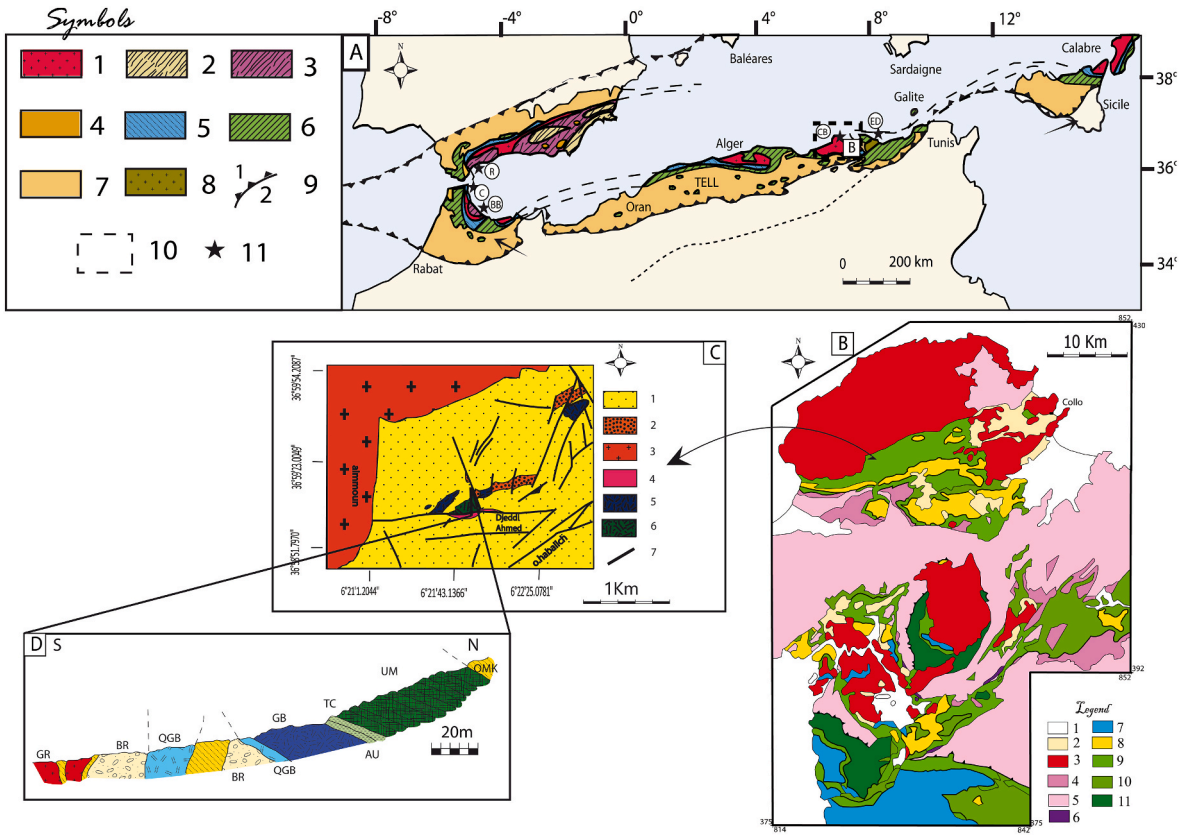

Fig. 1. (A) Sketch map of the alpine belt in the western Mediterranean area (Durand-Delga, 1980). 1. Former massifs Betic-Rif, Kabylies, Peloritan and Calabrese; 2. Nevado-Filabride (Andalusia) and Palaeozoic Permo-Triassic submitted to Alpine metamorphism; 3. Alpujarrides (Andalusia) and Sebtides (Rif): Paleozoic slightly or not metamorphic; 4. Malaguide (Andalusia) and Ghomarides (Rif): Paleozoic metamorphic and little or no coverage; 5. Mesozoic limestone ridge (Betic, Rif, Kabylies); 6. Flysch (Cretaceous and Paleogene) allochthonous External Zones (African domain); 7. External Rif and Algerian Tell (Mesozoic and Cenozoic); 8. Former Massif (Edough); 9. Front carted sets (1: 2 visible: hidden); 10. Area of B; 11. Mafic/Ultramafic localities: R – Ronda Massif; C – Ceuta Massif; BB – Beni Bousera Massif; CB: Cap Bougaroun Massif; ED: Edough Massif. (B) Geological sketch map of the Cap Bougaroun area (after Bouillin, 1977) 1. Quaternary; 2. Miocene post thrust sheet; 3. Eruptive Miocene; 4. Oligo-Miocene Kabyle; 5. Kabylian basement; 6. Tellian Triassic; 7. Tellian unit; 8. Numidian thrust sheets; 9. Massylian thrust sheets; 10. Mauritanian thrust sheets; 11. Mauritanian base. (C) Schematic outcrop of mafic and ultramafic rocks of the Yaddene Complex (after Bouillin, 1977). 1. hornfels of "Oligo-Miocene Kabyle"; 2. Numidian Sandstones; 3. Cap Bougaroun granite; 4. Microgranite; 5. Dolerite; 6. Layered massif of Yaddene; 7. Faults. (D) Cross section of ultramafic and mafic rocks from the Yaddene layered complex. UM: Ultramafic rocks; TC: Troctolite; AU: Augitite; GB: Gabbro; QGB: Quartz-bearing Gabbro; OMK: Oligo-Miocene Kabyle; GR: Granite; BR: Fault breaching.

of oceanic crust, such as the Liguro-Provençal basin, the Tyrrhenian Sea, or the Algerian Basin (Abbassene et al., 2001, 2016; Romagny et al., 2020; van Hinsbergen et al., 2020). Determining the age at which these back-arc basins opened is paramount for pinpointing the different geodynamic stages of the western Mediterranean, but such studies are limited. Very few works have been performed on the syn-opening sediments of these basins (Duggen et al., 2005; Speranza et al., 2002), but, till date, they have not been conducted on parental magmas accompanying the rifting stage of these basins. Samples from offshore drilling cores potentially allow dating the oceanic crust (e.g., Speranza et al., 2002), but dating the earliest stages of extension onshore is difficult. Syn-rift successions often contain rare biostratigraphic markers and display certain lateral facies variations that hamper the correlation and establishment of syn-rift stratigraphy. Thus, dating the initiation of extension, which ultimately leads to the opening of oceanic basins, is challenging. Mafic and ultramafic bodies are often emplaced in the continental crust during its breakup and extension (e.g., Roda et al., 2019), and can be used to explore the earliest stages of an extensional regime.

In this study, we focus on mafic and ultramafic rocks from the Yaddene layered complex that are intercalated within the syn-rift "Oligo-Miocene Kabyle" (OMK) series outcropping in the Collo area of Lesser Kabylia (NE Algeria). We provide petrographic observations, geochemical (major and trace elements) and geochronological analyses, and thermodynamic calculations of mafic and ultramafic rocks from this complex. The integration of these data and their interpretation give a better understanding of the genesis of these rocks and allow to propose a more precise geodynamic evolution of the first stages of the Algerian basin opening, which is a key step in the evolution of the Western Mediterranean.

2. Geological setting

The Maghrebide Belt, a young alpine orogenic system that extends from Morocco to Tunisia (Fig. 1a), borders the northern margin of Africa. The belt is connected to the eastern Apennines through the Sardinia Canal and in the west to the Betic Cordillera across the Gibraltar Strait and the Alboran Sea (Durand-Delga, 1980; Frizon de Lamotte et al., 2000). This orogenic system preserves fragments of continental and oceanic crust that were amalgamated during the Cenozoic. The most important feature in northern Algeria are the crystalline basement rocks (Greater and Lesser Kabylia), which represent the paleo-European margin (parts of the *AlKaPeCa* terrane of Bouillin, 1986) that docked to Africa. The Collo area, where the Yaddene complex is located, forms a large part (850 km^2) of Lesser Kabylia (Fig. 1b). The region is made of the Lesser Kabylia crystalline basement, composed of high-grade gneisses underlying low-grade micaschists and phyllites (Mahdjoub and Merle, 1990; Mahdjoub, 1991; Mahdjoub et al., 1997; Peucat et al.,

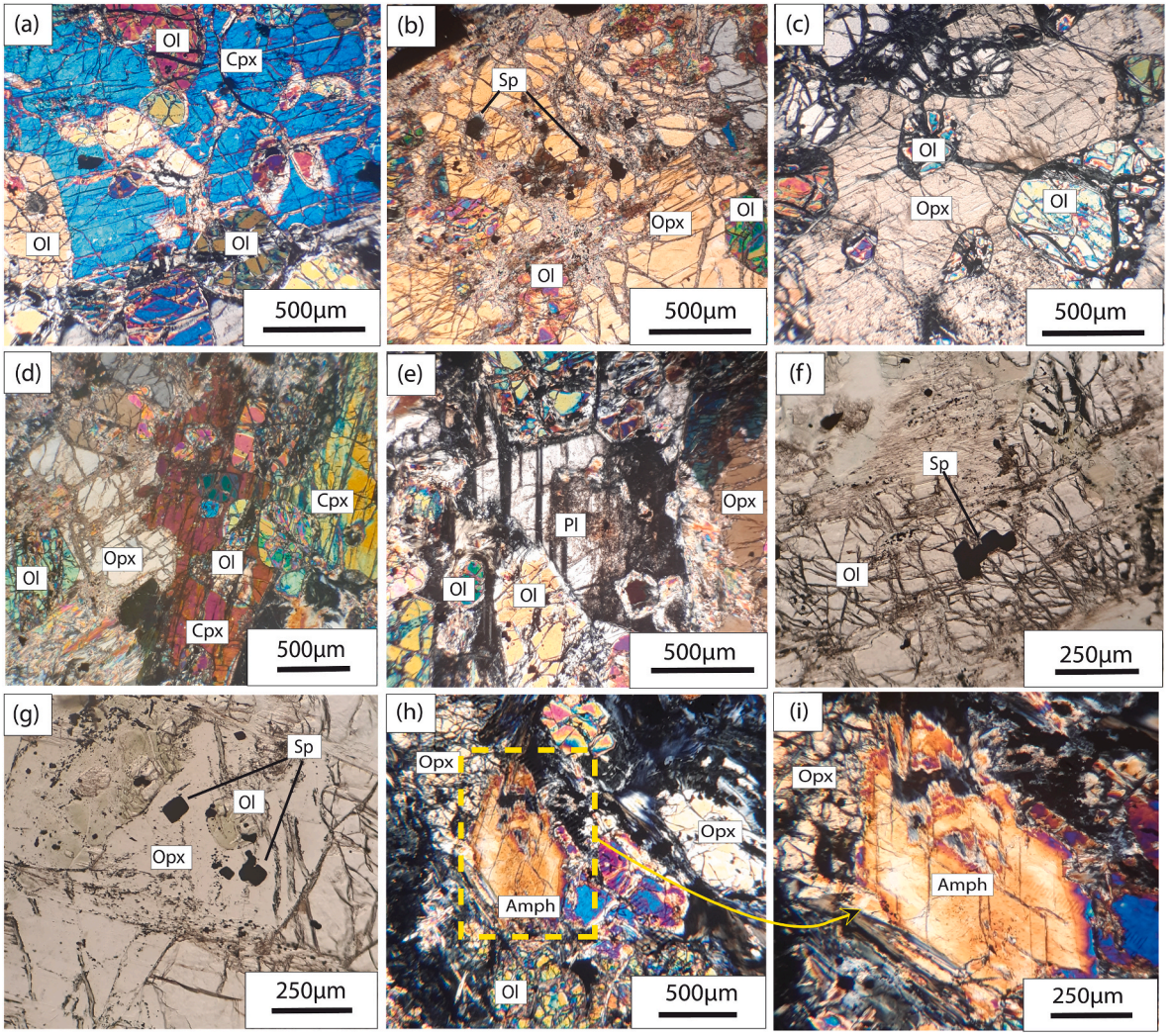

Fig. 2. Photomicrographs of thin sections from Plagioclase bearing lherzolite of Yaddene. (a) host clinopyroxene enclose olivine crystals (b) and (c) host orthopyroxène enclose olivine crystals. In (a),(b),&(c) the pyroxenes show neither deformation structures nor exsolution laminae. (d) pyroxenes sharing the same borders, fractured with no lamellae exsolutions and enclose olivine crystals (e) xenomorphic plagioclase with olivine inclusion (f) spinel occurs as euhedral crystals (octahedral) in the olivine (g) spinel inclusions in pyroxenes (h) et (i) primary amphibole shares borders with orthopyroxenes and olivine.

1996). The age of the Lesser Kabylian basement is not known; however, the Edough massif situated further east underwent high-grade metamorphism at 275–315 Ma (Bruguier et al., 2009; Fernandez et al., 2016). These ages are similar to those from the Kabylian basement in Greater Kabylia situated further west, where the Variscan basement underwent granulite facies metamorphism at 275–285 Ma (Peucat et al., 1996; Mahdjoub et al., 1997; Hammor et al., 2006). This crystalline basement unconformably overlies several alpine nappes in the Collo area, and are made of the following units from bottom to top: i) the Tellian unit, which comprises Mesozoic and Tertiary sediments of African affinity and are overthrusted by the Flysch unit; ii) the Flysch unit, which consists mainly of Cretaceous to Eocene flysch, composed of turbiditic sandstones deposited in the East Ligurian Tethys between the *AlKaPeCa* domains and the African margin. The flysch are subdivided into two main units: Massylian and Mauritanian flyschs (Gelard, 1969; Raoult, 1969; Bouillin et al., 1970). The Massylian flysch comprises an Albian–Aptian quartzo-pelitic series covered by a pelitic microbreccia series of the Upper Cretaceous age. The Mauritanian flysch is composed of carbonates and red radiolarites of the Dogger-Malm overlain by Cretaceous to Paleocene conglomerates, sandstones, and carbonates. The Mauritanian flysch is sourced from the north (*AlKaPeCa* terranes), whereas the Massylian flysch is derived from the south (African foreland) (Belayouni et al. (2013); iii) Paleozoic-Mesozoic unmetamorphosed carbonates and sediments that overthrust the abovementioned units and are known as the "dorsale calcaire" (Dorsale Kabyle; Durand-Delga, 1969).

The crystalline basement of Lesser Kabylia is unconformably overlain by the OMK clastic sediments, which represent an upward-thinning transgressive sedimentary sequence, beginning with Upper Oligocene/Lower Aquitanian alluvial conglomerates at the base. These are overlain by micaceous sandstones capped by fine-grained sediments (shales and silexites), reflecting a more marine environment. The silexites are Aquitanian in age (Géry et al., 1981). The upper part of the OMK is overlain by olistostromes (tectono-sedimentary formation with flysch debris and olistoliths) of Burdigalian age (Bouillin, 1977; Wildi, 1983). The basal conglomerates and fine-grained sediments have been interpreted as a syn-rift material deposited coevally at the onset of opening of the Algerian back-arc basin (Arab et al., 2016). The series records a widespread Upper Oligocene/Lower Miocene extensional regime that affected the entire area, and was related to the rifting stage of the Algerian marginal basin (Leprêtre et al., 2018). This is consistent with seismic data (Arab et al., 2016), which identified offshore sedimentary units (PMSU1), which are possible lateral equivalent to onshore OMK, resting directly on the basement in the continental to transitional

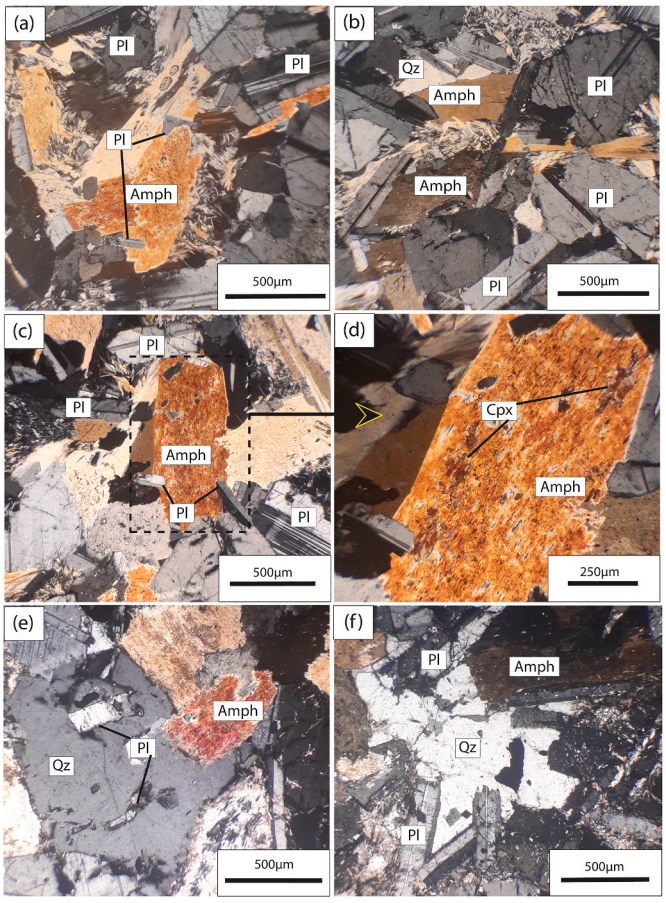

Fig. 3. Photomicrographs of thin sections from quartz-bearing gabbro of Yaddene.(a),(b),& (c) intergranular texture where the spaces between plagioclase laths are occupied by clinopyroxene grains (mostly altered to actinolite) (d) enlarged amphiboles from the photomicrograph (c) where amphibole contain relics of clinopyroxene indicate that these amphibole are the result of the alteration of almost all clinopyroxene. (e), & (f) xenomorphic quartz contains plagioclase and amphibole inclusions and it bends the last interstice between the plagioclase and the amphibole.

domain of the Algerian Basin.

The mafic and ultramafic rocks of the Yaddene complex are located ~1 km south of the Cap Bougaroun granite and were first described by Bouillin and Kornprobst (1974) and later studied by Ouabadi (1994) and Abbassene et al. (2016) (Fig. 1c). Approximately 100 m thick mafic and ultramafic rocks (Fig. 1d) were found within the fine-grained sediments of the upper part of the OMK units. The rocks comprise undeformed lherzolite at the top, with gabbros and quartz-bearing gabbros occurring at the bottom and separated from the ultramafic rocks by troctolites and augitites. The complex was interpreted by Bouillin and Kornprobst (1974) as a stratified magmatic complex emplaced within the argillaceous sediments of the OMK and resulting from the low-pressure (<3 kbar) fractional crystallization of a tholeiitic magma. The OMK rocks in this area have been metamorphosed at their contact with the 17 Ma Cap Bougaroun granite (Abbassene et al., 2016), suggesting that the Yaddene complex is older than Upper Burdigalian.

3. Petrography

The studied rocks were sampled from the valley of Mechta Yaddene (Fig. 1d), where they are represented from north to south by the following lithologies: i) plagioclase-bearing lherzolites (CB38, CB34); ii) troctolites and augitites; and iii) quartz-bearing gabbros (CB39, CB36).

3.1. Ultramafic rocks

Representative samples of plagioclase-bearing lherzolites (CB38 and CB34) were collected from the study area. The rocks are medium-to coarse-grained (3–5 mm) and show poikilitic texture (cumulate texture), with large crystals of orthopyroxene and clinopyroxene, enclosing a number of randomly oriented and uniformly distributed olivine and chromian spinel crystals (Fig. 2a–d). They are composed of olivine (50–55%), orthopyroxene (5–10%), clinopyroxene (30–40%), plagioclase (5–10%), and chromian spinel (up to 5%). Olivine, often fractured, occurs as subhedral aggregates displaying sizes in the range 0.3–0.7 mm. It is often found as inclusions in pyroxene crystals. The host pyroxenes are of 3–4 mm in size and are usually fractured showing no lamellae exsolutions (Fig. 2a–d). Plagioclase (1 mm in size) occurs as interstitial xenomorphic crystals (Fig. 2e). Cr-spinel is the most common accessory phase. It generally occurs as euhedral crystals (octahedral) in the olivine aggregates, but rare occurrences have also been observed in pyroxenes (Fig. 2f and g). Amphibole is observed for the first time in the plagioclase-bearing lherzolites from Yaddene complex. As a primary phase, the amphibole shows euhedral crystals with the typical diamond-shaped cleavages at about 60° and 120° (Fig. 2h and i).

3.2. Mafic rocks

The studied mafic rocks of the Yaddene complex are represented by layered coarse-to fine-grained (1–3 mm) quartz-bearing gabbros (samples CB36 and CB39). Microscopically, they are composed of plagioclase (65–75%), clinopyroxene (15–20%) (severely altered to actinolite), and quartz (5–10%), and display an intergranular texture. Actinolite (after pyroxene) is often interstitial between the plagioclase (Fig. 3a–c). Plagioclase occurs as large euhedral to subhedral crystals of 0.5–1 mm in size that are often arranged subradial or subparallel to each other and partially enclosed by amphibole (Fig. 3a–c). Secondary amphibole occurs as large (1.0–1.5 mm) subhedral crystals (Fig. 3c). Some of them contain relics of clinopyroxene indicating that these pseudomorphic amphiboles are the result of replacement of clinopyroxene (uralitization) (Fig. 3d) in the mafic rocks. Quartz is xenomorphic and contains plagioclase and amphibole inclusions and it bends the last interstice between the plagioclase and the amphibole (Fig. 3e and f). This interstitial quartz expresses an oversaturation of primary magma in silica.

4. Analytical technique

4.1. Mineral chemistry

Major element chemical composition of the minerals was determined with an electron probe microanalyzer (EPMA) using the CAMECA SX100 equipped with five wavelength dispersive X-ray spectrometers at the University of Montpellier, France. Analyses were performed using an accelerating voltage of 20 kV, a beam current of 10 nA, a beam diameter of 1 µm, and counting time of 30 s.

Selected minerals were analyzed for trace elements using laser ablation inductively coupled plasma mass spectrometry (LA-ICP-MS) at Géosciences Montpellier (University of Montpellier, AETE-ISO regional facility of the OSU OREME). Analyses were performed using a Teledyne G2 excimer laser operating at 193 nm, equipped with a Helex II two-volume sample cell. The laser system was coupled to a ThermoFinnigan Element XR double-focusing magnetic sector field ICP-MS. The instrument was tuned to achieve the maximum sensitivity and low oxide production (ThO/Th <1%). Ablation was conducted under ultra-pure helium, which enhanced sensitivity and reduced inter-element fractionation (Günther and Heinrich, 1999). The helium gas stream and ablated material were then mixed with small amounts of pure nitrogen, and subsequently with argon, before entering the plasma source. The laser was operated at a frequency of 5 Hz and energy density of 5 J/cm^2 using a 65 µm spot size. The total analysis time was 120 s with the first

Table 1
Major element compositions of minerals (amphibole, clinopyroxene, Cr-spinel, olivine, orthopyroxene and plagioclase) from rocks of the Yaddene complex (Lesser Kabylia, NE Algeria).

mineral type	Cr-Spinel						
Rock type	Plagioclase bearing lherzolite						
sample name	CB 34					CB 38	
Major elements (wt%)							
SiO2	0.20	1.76	0.20	0.25	0.27	0.18	0.24
TiO2	0.28	0.25	1.09	0.27	0.25	1.92	1.37
Al2O3	13.11	13.62	13.48	12.42	12.88	12.15	12.91
Cr2O3	47.06	42.74	44.34	49.88	49.69	42.47	44.43
NiO	0.09	0.07	0.11	0.06	0.07	0.13	0.14
FeOt	28.34	29.95	29.50	26.00	25.83	31.38	30.55
MnO	0.40	0.41	0.40	0.44	0.41	0.39	0.39
MgO	7.26	7.19	7.90	8.29	8.34	8.13	7.87
CaO	0.06	0.01	0.08	0.01	0.00	0.01	0.02
TOTAL	97.52	96.66	97.94	98.21	98.30	97.82	99.77
Si	0.06	0.48	0.05	0.07	0.07	0.05	0.06
Ti	0.06	0.05	0.22	0.06	0.05	0.39	0.28
Al	4.20	4.37	4.28	3.94	4.07	3.88	4.08
Cr	10.12	9.21	9.44	10.62	10.54	9.10	9.41
Ni	0.06	0.05	0.07	0.04	0.05	0.09	0.09
Fe	6.45	6.82	6.65	5.85	5.79	7.11	6.84
Mn	0.09	0.09	0.09	0.10	0.09	0.09	0.09
Mg	2.95	2.92	3.17	3.33	3.33	3.29	3.14
Ca	0.02	0.00	0.02	0.00	0.00	0.00	0.01
TOTAL	24.00	24.00	24.00	24.00	24.00	24.00	24.00
Cr/Cr + Al	0.71	0.68	0.69	0.73	0.72	0.70	0.70
#Mg (Mg/(Mg + Fe))	0.31	0.30	0.32	0.36	0.37	0.32	0.31

mineral type	Olivine										
Rock type	plagioclase bearing lherzolite										
sample name	CB 34							CB 38			
Major elements (wt%)											
SiO2	40.65	40.59	39.91	40.03	40.59	40.67	40.30	40.43	40.45	39.95	40.30
TiO2	0.01	bdl	0.01	0.005	0.01	0.02	bdl	0.02	0.03	0.02	bdl
Al2O3	bdl	0.005	0.010	0.002	0.003	0.012	bdl	0.031	0.000	0.021	bdl
Cr2O3	0.03	0.03	0.05	0.02	0.00	0.04	0.05	0.02	0.02	bdl	bdl
FeO	10.71	12.11	12.84	12.09	11.44	12.67	11.79	12.56	12.01	12.44	12.20
MnO	0.17	0.17	0.17	0.19	0.17	0.17	0.17	0.18	0.19	0.21	0.20
MgO	46.86	46.08	45.80	46.17	46.51	45.63	46.23	46.01	46.17	45.99	45.98
NiO	0.26	0.25	0.27	0.25	0.29	0.28	0.26	0.28	0.27	0.29	0.29
CaO	0.13	0.14	0.15	0.14	0.15	0.09	0.15	0.14	0.12	0.12	0.10
TOTAL	98.82	99.38	99.20	98.88	99.16	99.59	98.95	99.66	99.27	99.03	99.07
Si	1.01	1.01	1.00	1.00	1.01	1.01	1.01	1.01	1.01	1.00	1.01
Ti	0.00	0.00	0.00	0.00	0.00	0.00	0.00	0.00	0.00	0.00	0.00
Al	0.00	0.00	0.00	0.00	0.00	0.00	0.00	0.00	0.00	0.00	0.00
Cr	0.00	0.00	0.00	0.00	0.00	0.00	0.00	0.00	0.00	0.00	0.00
Fe	0.22	0.25	0.27	0.25	0.24	0.26	0.25	0.26	0.25	0.26	0.26
Mn	0.00	0.00	0.00	0.00	0.00	0.00	0.00	0.00	0.00	0.00	0.00
Mg	1.74	1.71	1.71	1.73	1.73	1.70	1.73	1.71	1.72	1.72	1.72
Ni	0.01	0.01	0.01	0.00	0.01	0.01	0.01	0.01	0.01	0.01	0.01
Ca	0.00	0.00	0.00	0.00	0.00	0.00	0.00	0.00	0.00	0.00	0.00
TOTAL	2.99	2.99	3.00	3.00	2.99	2.99	2.99	2.99	2.99	3.00	2.99
#Mg (Mg/(Mg + Fe))	0.89	0.87	0.86	0.87	0.88	0.87	0.87	0.87	0.87	0.87	0.87
Fo	88.47	86.99	86.26	87.02	87.71	86.36	87.33	86.56	87.09	86.63	86.86
Fa	11.35	12.82	13.56	12.78	12.10	13.45	12.49	13.25	12.71	13.15	12.93

mineral type	Orthopyroxene									
Rock type	Plagioclase bearing lherzolite									
sample name	CB 34			CB 38						
Major elements (wt%)										
SiO2	53.830	55.618	55.355	55.711	55.167	55.378	54.893	55.412	55.127	56.781
TiO2	0.215	0.131	0.255	0.217	0.150	0.165	0.165	0.322	0.266	0.137
Al2O3	2.203	2.087	1.939	1.658	2.281	1.864	2.190	1.628	1.724	0.774
Cr2O3	0.522	0.205	0.476	0.458	0.591	0.480	0.595	0.402	0.467	0.166
NiO	0.046	0.075	0.088	0.072	0.074	0.063	0.079	0.084	0.083	0.096
FeOt	8.206	8.249	8.369	8.214	7.748	7.887	7.965	8.209	7.974	7.946

(*continued on next page*)

Table 1 (*continued*)

mineral type	Orthopyroxene									
Rock type	Plagioclase bearing lherzolite									
sample name	CB 34			CB 38						
MnO	0.189	0.187	0.195	0.178	0.180	0.173	0.165	0.226	0.195	0.178
MgO	30.717	30.997	30.928	31.417	31.239	31.032	30.874	31.110	30.928	31.525
CaO	1.528	1.740	1.642	1.575	1.664	1.912	1.705	1.468	1.579	1.720
Na2O	bdl	0.025	0.011	0.017	0.010	bdl	0.054	0.009	0.002	0.022
K2O	bdl	bdl	bdl	bdl	bdl	bdl	bdl	0.002	0.001	bdl
TOTAL	97.520	99.315	99.258	99.517	99.103	98.952	98.684	98.870	98.346	99.345
Si	1.932	1.959	1.954	1.958	1.944	1.957	1.945	1.962	1.961	1.998
Altot	0.093	0.087	0.081	0.069	0.095	0.078	0.092	0.068	0.072	0.032
Ti	0.006	0.003	0.007	0.006	0.004	0.004	0.004	0.009	0.007	0.004
Cr	0.015	0.006	0.013	0.013	0.016	0.013	0.017	0.011	0.013	0.005
Ni	0.001	0.002	0.002	0.002	0.002	0.002	0.002	0.002	0.002	0.003
Fe3+	0.017	0.000	0.000	0.000	0.000	0.000	0.000	0.000	0.000	0.000
Fe2+	0.229	0.243	0.247	0.241	0.228	0.233	0.236	0.243	0.237	0.234
Mn	0.006	0.006	0.006	0.005	0.005	0.005	0.005	0.007	0.006	0.005
Mg	1.643	1.627	1.627	1.646	1.641	1.635	1.631	1.642	1.640	1.653
Ca	0.059	0.066	0.062	0.059	0.063	0.072	0.065	0.056	0.060	0.065
Na	bdl	0.002	0.001	0.001	0.001	bdl	0.004	0.001	0.000	0.002
K	bdl	bdl	bdl	bdl	bdl	bdl	bdl	0.000	0.000	bdl
TOTAL	4.000	4.000	4.000	4.000	4.000	4.000	4.000	4.000	4.000	4.000
#Mg (Mg/(Mg + Fe))	0.878	0.870	0.868	0.872	0.878	0.875	0.874	0.871	0.874	0.876
Wo	0.030	0.034	0.032	0.030	0.033	0.037	0.034	0.029	0.031	0.033
En	0.851	0.841	0.840	0.845	0.849	0.843	0.844	0.846	0.846	0.847
Fs	0.119	0.126	0.128	0.124	0.118	0.120	0.122	0.125	0.122	0.120

mineral type	Clinopyroxenes							
Rock type	Plagioclase bearing lherzolite							
sample name	CB 34		CB 38					
Major elements (wt%)								
SiO2	52.58	52.83	52.79	53.07	52.12	52.13	52.12	52.22
TiO2	0.17	0.34	0.22	0.20	0.20	0.16	0.19	0.14
Al2O3	2.32	2.12	1.84	1.83	2.69	2.37	2.52	2.27
Cr2O3	0.80	0.69	0.51	0.57	0.97	0.83	0.80	1.04
NiO	0.01	0.03	0.03	0.03	0.04	0.01	0.05	0.05
FeOt	3.44	3.87	3.58	3.75	3.55	3.28	3.42	3.33
MnO	0.10	0.17	0.14	0.11	0.11	0.12	0.11	0.10
MgO	17.91	17.42	16.79	18.51	17.72	17.67	17.68	17.90
CaO	21.66	21.62	22.98	21.10	21.16	21.60	21.38	21.56
Na2O	0.09	0.14	0.18	0.09	0.12	0.07	0.11	0.08
K2O	bdl	bdl	bdl	bdl	bdl	bdl	bdl	bdl
TOTAL	99.16	99.25	99.15	99.35	98.72	98.28	98.43	98.77
Si	1.93	1.94	1.94	1.94	1.92	1.93	1.92	1.92
Altot	0.10	0.09	0.08	0.08	0.12	0.10	0.11	0.10
Ti	0.00	0.01	0.01	0.01	0.01	0.00	0.01	0.00
Cr	0.02	0.02	0.01	0.02	0.03	0.02	0.02	0.03
Ni	0.00	0.00	0.00	0.00	0.00	0.00	0.00	0.00
Fe3+	0.02	0.00	0.02	0.02	0.01	0.01	0.02	0.02
Fe2+	0.09	0.12	0.09	0.09	0.10	0.09	0.09	0.08
Mn	0.00	0.01	0.00	0.00	0.00	0.00	0.00	0.00
Mg	0.98	0.95	0.92	1.01	0.97	0.97	0.97	0.98
Ca	0.85	0.85	0.91	0.83	0.84	0.86	0.85	0.85
Na	0.01	0.01	0.01	0.01	0.01	0.00	0.01	0.01
K	bdl	bdl	bdl	bdl	bdl	bdl	bdl	bdl
TOTAL	4.00	4.00	4.00	4.00	4.00	4.00	4.00	4.00
#Mg (Mg/(Mg + Fe))	0.92	0.89	0.91	0.92	0.91	0.92	0.92	0.93
Wo	44.41	44.25	47.28	42.87	43.87	44.63	44.31	44.52
En	4.51	6.15	4.68	4.82	5.05	4.60	4.73	4.08
Fs	51.08	49.60	48.04	52.31	51.08	50.78	50.96	51.40

mineral type	Plagioclase									
Rock type	Quartz bearing gabbro									
sample name	CB 36									
Major elements (wt%)										
SiO2	44.11	43.85	44.20	45.13	44.04	44.08	44.12	44.62	44.18	44.35
TiO2	0.01	0.00	0.00	0.00	0.04	0.00	0.01	0.01	0.00	0.00

(*continued on next page*)

Table 1 (*continued*)

mineral type	Plagioclase									
Rock type	Quartz bearing gabbro									
sample name	CB 36									
Al2O3	34.74	34.97	34.89	35.27	34.83	34.67	34.68	34.55	34.46	34.88
Cr2O3	0.00	0.02	0.00	0.03	0.00	0.00	0.01	0.01	0.00	0.00
FeOt	0.35	0.48	0.36	0.57	0.31	0.45	0.38	0.41	0.42	0.36
MnO	0.00	0.01	0.01	0.00	0.01	0.00	0.02	0.00	0.02	0.01
MgO	0.12	0.01	0.08	0.02	0.13	0.05	0.09	0.10	0.10	0.08
NiO	0.02	0.02	0.00	0.02	0.03	0.00	0.00	0.00	0.00	0.01
CaO	19.11	19.10	19.33	19.31	19.17	19.08	19.03	19.09	19.20	19.18
Na2O	0.65	0.64	0.64	0.68	0.56	0.73	0.70	0.75	0.70	0.67
K2O	0.01	0.02	0.01	0.02	0.00	0.01	0.02	0.02	0.01	bdl
TOTAL	99.12	99.12	99.52	101.06	99.13	99.07	99.07	99.54	99.09	99.53
Si	2.06	2.05	2.06	2.07	2.06	2.06	2.06	2.07	2.07	2.06
Al	1.91	1.93	1.91	1.91	1.92	1.91	1.91	1.89	1.90	1.91
Ti	0.00	0.00	0.00	0.00	0.00	0.00	0.00	0.00	0.00	0.00
Cr	0.00	0.00	0.00	0.00	0.00	0.00	0.00	0.00	0.00	0.00
Fe2+	0.01	0.02	0.01	0.02	0.01	0.02	0.01	0.02	0.02	0.01
Mn	0.00	0.00	0.00	0.00	0.00	0.00	0.00	0.00	0.00	0.00
Mg	0.01	0.00	0.01	0.00	0.01	0.00	0.01	0.01	0.01	0.01
Ni	0.00	0.00	0.00	0.00	0.00	0.00	0.00	0.00	0.00	0.00
Ca	0.96	0.96	0.96	0.95	0.96	0.96	0.95	0.95	0.96	0.96
Na	0.06	0.06	0.06	0.06	0.05	0.07	0.06	0.07	0.06	0.06
K	0.0006	0.0012	0.0005	0.0010	0.0002	0.0009	0.0013	0.0010	0.0009	bdl
totale	5.01	5.02	5.01	5.01	5.01	5.02	5.01	5.01	5.02	5.01
XAn	0.94	0.94	0.94	0.94	0.95	0.93	0.94	0.93	0.94	0.94
XAlb	0.06	0.06	0.06	0.06	0.05	0.06	0.06	0.07	0.06	0.06
XOrth	0.00	0.00	0.00	0.00	0.00	0.00	0.00	0.00	0.00	0.00

mineral type	Amphibole									
Rock type	Quartz bearing gabbro							Plagioclase bearing lherzolite		
sample name	CB 36							CB34		CB38
Major elements (wt%)										
SiO2	54.59	54.89	55.90	52.84	54.72	54.09	49.24	46.12	45.67	44.82
TiO2	0.27	0.21	0.13	0.65	0.05	0.15	0.65	1.28	0.50	1.76
Al2O3	1.48	2.39	1.56	2.97	1.54	2.52	3.69	9.16	10.53	11.15
Cr2O3	0.02	0.21	0.02	0.00	0.04	0.32	0.02	1.53	1.29	1.53
FeOt	12.85	6.92	7.82	13.76	11.08	8.02	20.69	5.36	5.28	4.69
MnO	0.29	0.18	0.21	0.29	0.24	0.19	0.26	0.07	0.10	0.10
MgO	14.82	18.35	18.14	13.67	16.10	17.85	10.14	17.93	18.18	17.73
CaO	12.30	13.15	12.34	12.40	12.91	12.62	10.91	11.62	11.66	11.43
Na2O	0.12	0.12	0.12	0.14	0.06	0.16	0.71	2.46	2.62	2.69
K2O	0.03	0.02	0.03	0.05	0.03	0.04	0.28	0.52	0.24	0.18
H2O*	2.07	2.11	2.11	2.05	2.08	2.09	1.97	2.07	2.07	2.10
Total	98.84	98.61	98.40	98.82	98.84	98.07	98.54	98.20	98.22	99.27
T (ideally 8 apfu)										
Si	7.92	7.79	7.94	7.72	7.88	7.80	7.72	6.80	6.79	6.61
Al	0.08	0.21	0.06	0.28	0.12	0.20	0.28	1.20	1.21	1.39
C (ideally 5 apfu)										
Ti	0.03	0.02	0.01	0.07	0.01	0.02	0.08	0.14	0.06	0.20
Al	0.17	0.19	0.20	0.23	0.14	0.23	0.40	0.39	0.63	0.55
Cr	0.00	0.02	0.00	0.00	0.00	0.04	0.00	0.18	0.15	0.18
Mn2+	0.04	0.02	0.01	0.04	0.03	0.02	0.04	0.01	0.01	0.01
Fe2+	1.56	0.82	0.93	1.68	1.34	0.84	2.01	0.27	0.01	0.07
Mg	3.20	3.88	3.84	2.98	3.46	3.84	2.37	3.94	4.03	3.90
B (ideally 2 apfu)										
Ca	1.91	2.00	1.88	1.94	1.99	1.95	1.83	1.84	1.86	1.81
Na	0.03	0.00	0.03	0.04	0.01	0.04	0.17	0.17	0.14	0.19
A (from 0 to 1 apfu)										
Na		0.03			0.01		0.05	0.54	0.61	0.58
K	0.01	0.00	0.01	0.01	0.01	0.01	0.06	0.10	0.05	0.03
W (ideally 2 apfu)										
OH	2.00	2.00	2.00	2.00	2.00	2.00	2.00	2.00	2.00	2.00
#Mg (Mg/(Mg + Fe))	0.67	0.83	0.81	0.64	0.72	0.80	0.47	0.86	0.86	0.87

80 s used for background measurements before sample ablation. Synthetic glass (NIST 612) was used for external calibration (values after Pearce et al., 1997). Internal standard normalization was performed using either CaO or SiO_2 and the corresponding values measured using the EPMA. Accuracy was monitored using the fused glass standard BIR-1G (values obtained after the Georem preferred values). Data reduction was performed using Glitter package software (van Achterberg, 2001).

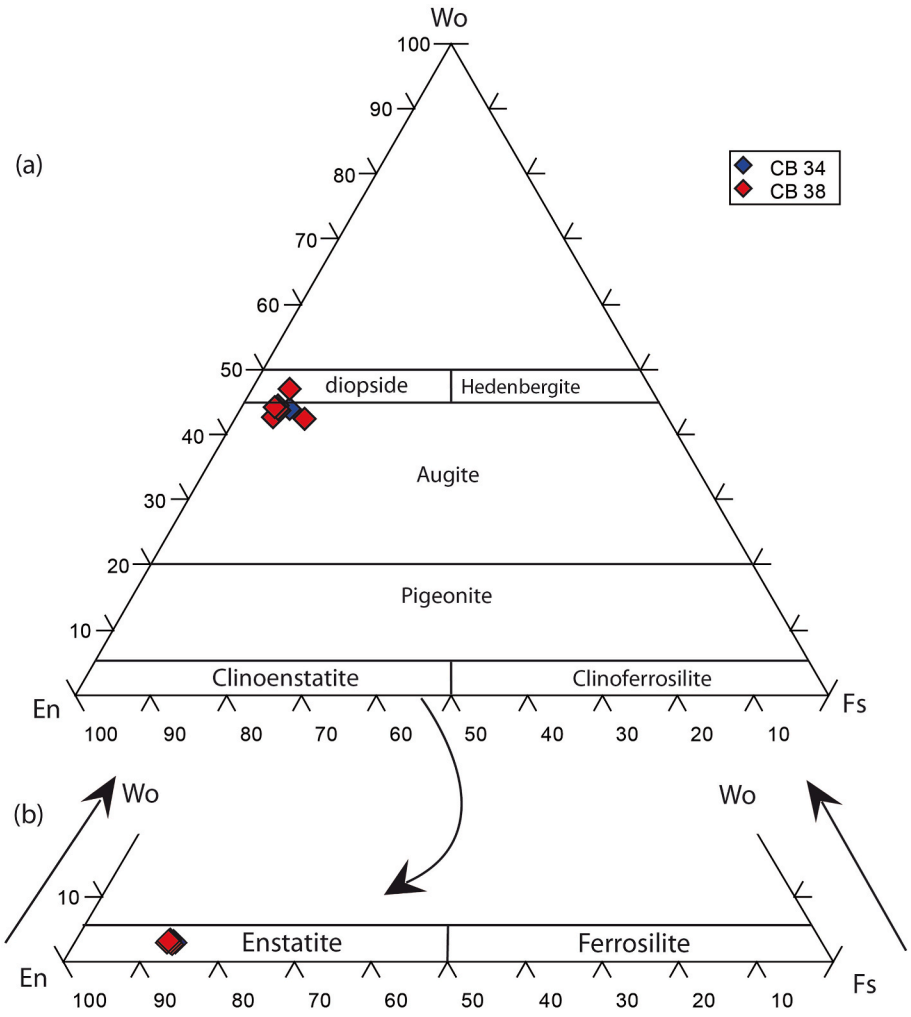

Fig. 4. En-Fs-Wo ternary diagram for pyroxene from lherzolite CB34 and CB38 (after Morimoto, 1988).

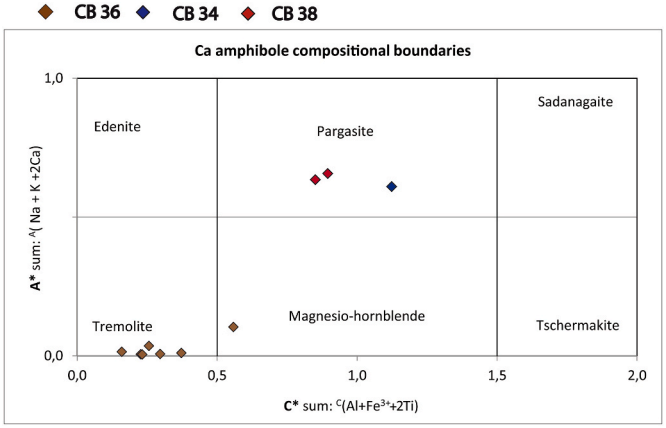

Fig. 5. Classification diagrams of amphibole (after: Hawthorne et al., 2012) from lherzolite CB34 and CB38 and quartz-bearing gabbro CB36.

4.2. U-Pb geochronology

U-Pb isotopic analyses were performed on zircon and titanite using the LA-ICP-MS equipment described above. The laser was operated at a frequency of 4 Hz and energy density of 5 J/cm^2 using a 20 μm spot size. For zircon, Pb/U and Pb/Pb ratios were calibrated against the reference material 91500 (Wiedenbeck et al., 1995), and GJ-1 (Jackson et al., 2004) was used as a secondary standard. For titanite, Pb/U and Pb/Pb ratios were calibrated against MKED1 (Spandler et al., 2016) and Khan Mine (Heaman, 2009) was used as a secondary standard to check for accuracy. Data were evaluated using the Glitter software (van Achterberg, 2001). Ages were calculated using the Isoplot/Ex add-in (Ludwig, 2003) and are quoted in the text at the 2σ level. Reproducibility of the Pb/U ratio was ±1.3% for 91500 and ± 1.0% for MKED1 (1sd) for the laser session required to analyze the samples. GJ-1 was analyzed along with the unknown samples and provided a $^{206}Pb/^{238}U$ age of 604.5 ± 3.4 Ma (n = 7), consistent with the reference value quoted in Jackson et al. (2004). Khan Mine titanite provided a $^{206}Pb/^{238}U$ age of 524.3 ± 4.6 Ma (n = 6), also consistent with the reference value reported by Heaman (2009).

4.3. Whole rocks geochemistry

The analyses of whole rocks (CB38, CB34, CB39, and CB36) used in this study are taken from the paper of Abbassene et al. (2016) and the thin sections observed and analyzed (CB38, CB34, CB39, and CB36) in this study were made from the same whole-rock samples.

5. Results

5.1. Mineral chemistry

Results of the major element chemistry of spinel, olivine,

Table 2
In-situ trace element analyses of minerals (clinopyroxene, olivine, orthopyroxene and plagioclase) from rocks of the Yaddene complex (Lesser Kabylia, NE Algeria).

mineral type		Clinopyroxene														
Rock type		plagioclase bearing lherzolite											Quartz bearing gabbro			
sample name	*LOD*	CB38			CB34								CB39			
trace elements (ppm)																
Ba	0.0025	0.0494	0.0173	0.198	0.0872	0.445	0.0953	0.132	0.191	0.143	0.358	0.0029	1.52	2.24	1.24	2.000
Rb	0.0008	0.0105	0.0049	0.0238	0.1123	0.122	0.0199	0.0131	0.1218	0.0433	0.0486	0.0016	0.206	0.252	0.278	0.416
Sr	0.0015	2.79	2.5	2.75	2.306	2.12	2.181	1.885	1.967	2.37	2.679	2.028	3.24	4.000	3.3	7.48
Pb	0.0015	0.1102	0.0556	0.139	0.328	0.710	0.1289	0.1359	0.591	0.0166	0.0563	N/A	0.843	0.995	0.655	1.28
Th	0.0001	0.00294	0.00248	0.00308	0.00253	0.0170	0.00446	0.00154	0.0134	0.00148	0.00103	N/A	0.154	0.137	0.123	0.151
U	0.0001	0.00043	0.00035	0.00083	0.00031	0.00565	0.00111	0.00038	0.00449	0.00040	0.00039	N/A	0.0249	0.0337	0.0277	0.0381
Ti	0.2289	1664.88	1057.14	1173.67	747.57	1253.02	720.02	1173.72	1105.39	1053.36	881.13	9486.14	725.48	1238.97	698.46	1175.35
Zr	0.0012	2.476	1.294	1.562	1.557	0.758	1.423	1.188	1.263	1.093	0.952	1.194	1.851	3.36	1.846	1.937
Nb	0.0005	0.0193	0.0184	0.0194	0.02	0.0202	0.0149	0.0197	0.0184	0.0146	0.0131	0.0152	0.0211	0.201	0.0334	0.0591
Ni	0.1450	304.46	309.22	311.26	302.12	401.61	286.45	340.59	354.56	331.99	293.27	298.73	152.43	158.62	155.25	156.99
Co	0.0110	31.44	31.13	32.31	30.1	39.06	28.1	33.63	34.09	31.25	28.19	28.78	47.63	48.72	46.08	45.87
Cr	0.1708	6956.9	–	7147.1	–	–	–	–	–	–	–	–	437.67	523.84	488.93	563.76
P	0.3360	59.78	57.69	61.49	52.31	51.6	50.19	48.23	56.14	53.23	55.28	141.36	52.31	51.6	50.19	48.23
La	0.0002	0.194	0.1351	0.1285	0.1234	0.1991	0.1356	0.105	0.1773	0.1104	0.0864	0.0932	0.235	0.522	0.207	0.293
Ce	0.0014	0.892	0.534	0.573	0.534	0.529	0.525	0.443	0.575	0.443	0.369	0.413	0.888	1.44	0.776	1.38
Pr	0.0002	0.188	0.115	0.121	0.1111	0.0833	0.1042	0.0997	0.1073	0.095	0.0821	0.0904	0.179	0.252	0.151	0.319
Nd	0.0002	1.228	0.749	0.792	0.776	0.548	0.743	0.66	0.684	0.632	0.558	0.602	1.096	1.47	0.963	1.95
Sm	0.0002	0.653	0.395	0.434	0.393	0.268	0.37	0.361	0.304	0.291	0.309	0.328	0.456	0.626	0.413	0.849
Eu	0.0007	0.228	0.135	0.157	0.146	0.1008	0.1315	0.1212	0.1086	0.1019	0.1006	0.1194	0.14	0.185	0.132	0.253
Gd	0.0004	1.16	0.662	0.721	0.681	0.506	0.655	0.612	0.612	0.583	0.497	0.607	0.73	0.919	0.64	1.2
Tb	0.0005	0.219	0.1319	0.1521	0.1383	0.0934	0.1293	0.1219	0.1254	0.1074	0.0974	0.1121	0.1355	0.171	0.1142	0.235
Dy	0.0001	1.679	0.989	1.104	1.086	0.694	0.977	0.922	0.987	0.845	0.734	0.9	0.99	1.26	0.844	1.61
Ho	0.0002	0.362	0.211	0.247	0.2123	0.1498	0.2078	0.2063	0.2194	0.1791	0.1573	0.1942	0.223	0.272	0.19	0.34
Er	0.0001	0.983	0.591	0.711	0.66	0.441	0.592	0.581	0.605	0.487	0.436	0.526	0.602	0.756	0.555	0.895
Tm	0.0002	0.1467	0.0873	0.1023	0.0921	0.0598	0.0839	0.0815	0.0948	0.0761	0.0647	0.0784	0.0895	0.1135	0.0832	0.1242
Yb	0.0002	0.929	0.563	0.653	0.567	0.46	0.549	0.563	0.624	0.462	0.424	0.52	0.582	0.798	0.58	0.751
Lu	0.0003	0.1308	0.0805	0.0926	0.0886	0.0671	0.0826	0.0843	0.0894	0.0662	0.06	0.0799	0.0847	0.132	0.0979	0.0918
Y	0.0008	8.51	5.04	5.82	5.46	3.86	5.2	5.01	5.21	4.22	3.83	4.62	5.25	6.6	4.86	8.12
Cs	0.0004	0.00205	0.00194	0.0115	0.2586	0.2041	0.0189	0.00834	0.0623	0.057	0.0392	0.00066	0.1092	0.1073	0.0973	0.157
Ta	0.0001	0.00128	0.0005	0.00021	0.00049	0.00021	0.00032	0.00015	0.00037	0.00016	0.00018	0.00035	0.0009	0.0115	0.00055	0.00327
Hf	0.0005	0.167	0.0856	0.1133	0.1015	0.0532	0.0929	0.074	0.0888	0.0658	0.0624	0.0828	0.0903	0.145	0.0887	0.0988
Eu/Eu*		0.80	0.81	0.13	0.86	0.84	0.82	0.79	0.77	0.82	0.78	0.78	0.74	0.75	0.79	0.77
LaN/YbN		0.14	0.16	0.19	0.15	0.29	0.17	0.13	0.19	0.12	0.14	0.14	0.27	0.44	0.24	0.26
LaN/SmN		0.19	0.22	0.23	0.20	0.47	0.23	0.18	0.37	0.18	0.20	0.18	0.32	0.52	0.32	0.22
Sum_REE		8.99	5.38	2.88	5.61	4.20	5.29	4.96	5.31	4.66	4.82	3.98	6.43	8.92	5.75	10.29

mineral type	Orthopyroxene					Olivine		Plagioclase			
Rock type	plagioclase bearing lherzolite					plagioclase bearing lherzolite		Quartz bearing gabbro			
sample name	CB38					CB38		CB39			
trace elements (ppm)											
Ba	0.0049	0.05	0.0626	0.183	0.1142	bld	0.00093	3.89	4.85	4.29	5.02
Rb	0.0148	0.0619	0.086	0.1259	0.1385	0.00106	0.001	2.4	0.174	0.27	1.062
Sr	0.0352	0.0634	0.0836	0.1001	0.1151	0.0019	0.0018	77.33	90.47	88.01	94.64
Pb	0.0060	0.0359	0.0479	0.0535	0.0730	0.0019	0.0025	0.671	0.544	0.383	0.833
Th	0.00037	0.00013	0.00118	0.0104	0.0221	0.00003	bld	0.00160	0.00120	0.0087	0.0101
U	0.00008	0.00028	0.00103	0.00209	0.00301	0.00004	bld	0.00178	0.00020	0.00258	0.00048
Ti	1486.42	1381.81	1280.94	1549.63	1422.06	21.29	13.97	57.15	54.51	72.75	60.07
Zr	0.914	0.788	0.757	0.819	0.752	0.0169	0.0083	0.036	0.018	0.109	0.018
Nb	0.01202	0.013	0.01104	0.01283	0.00835	0.00032	0.00059	0.0052	0.0302	0.0143	0.00152

(*continued on next page*)

Table 2 (*continued*)

mineral type	Orthopyroxene					Olivine		Plagioclase			
Rock type	plagioclase bearing lherzolite					plagioclase bearing lherzolite		Quartz bearing gabbro			
sample name	CB38					CB38		CB39			
Ni	576.48	581.52	577.71	613.21	608.41	1983.42	1947.46	0.65	21.97	0.21	5.14
Co	65.74	66.79	65.72	67.55	67.67	157.69	155.63	0.43	6.53	0.354	1
Cr	4517.16	4413.62	4274.22	3700.46	2337.74	149.43	136.49	1.83	4.6	0.29	2.24
P	63.44	61.2	61	58.06	57.15	57.64	53.84	86.35	89.55	86.12	89.22
La	0.00607	0.0201	0.017	0.0169	0.052	0.00042	0.00019	0.291	0.183	0.234	0.305
Ce	0.0307	0.0506	0.0416	0.0394	0.087	0.00028	0.00087	0.513	0.339	0.416	0.557
Pr	0.00778	0.0093	0.00865	0.00675	0.0131	0.00015	0.00014	0.0555	0.0361	0.0423	0.0658
Nd	0.0658	0.0751	0.059	0.064	0.0802	0.00041	0.00084	0.233	0.128	0.202	0.352
Sm	0.0676	0.0572	0.0426	0.0537	0.0627	bld	0.00044	0.042	0.0353	0.055	0.0446
Eu	0.0252	0.0236	0.0217	0.0231	0.0215	bld	0.0005	0.184	0.156	0.148	0.179
Gd	0.202	0.156	0.133	0.143	0.154	0.0027	0.0033	0.0402	0.0288	0.0508	0.081
Tb	0.0522	0.0413	0.0367	0.0427	0.0449	0.00061	0.00148	0.0048	0.00337	0.0095	0.0184
Dy	0.507	0.426	0.355	0.397	0.425	0.019	0.0163	0.0383	0.0189	0.057	0.0707
Ho	0.133	0.1177	0.108	0.1174	0.122	0.00693	0.00497	0.006	0.0046	0.0074	0.0136
Er	0.483	0.435	0.388	0.424	0.439	0.0277	0.0225	0.0192	0.0107	0.0213	0.0266
Tm	0.093	0.0814	0.0743	0.0833	0.0758	0.00694	0.00452	0.00234	0.00134	0.00338	0.004
Yb	0.69	0.67	0.593	0.647	0.636	0.0592	0.0521	0.0141	0.0029	0.022	0.0172
Lu	0.1203	0.1141	0.1041	0.1109	0.1069	0.0097	0.0088	0.00121	0.0004	0.0046	0.00168
Y	3.44	3.04	2.74	3.01	3.14	0.1796	0.1636	0.184	0.0974	0.237	0.371
Cs	0.0544	0.137	0.236	0.1232	0.229	0.00052	0.00048	0.643	0.0389	0.0234	0.193
Ta	0.00041	0.00012	0.00019	0.00027	0.00034	0.00026	0.00012	0.0058	0.00036	0.00083	0.00079
Hf	0.0563	0.0493	0.0513	0.044	0.0393	0.0006	0.0007	0.00121	0.00088	0.0045	0.0011
Eu/Eu*	0.66	0.76	0.02	0.02	0.67	–	–	13.69	14.96	8.56	9.11
LaN/YbN	0.01	0.02	0.25	0.20	0.06	0.00	0.01	13.91	NA	7.17	11.96
LaN/SmN	0.06	0.22	0.02	0.02	0.52	–	–	4.36	3.26	2.68	4.30
Sum_REE	2.48	2.28	3.23	3.44	2.32	0.13	0.12	1.44	0.95	1.27	1.74

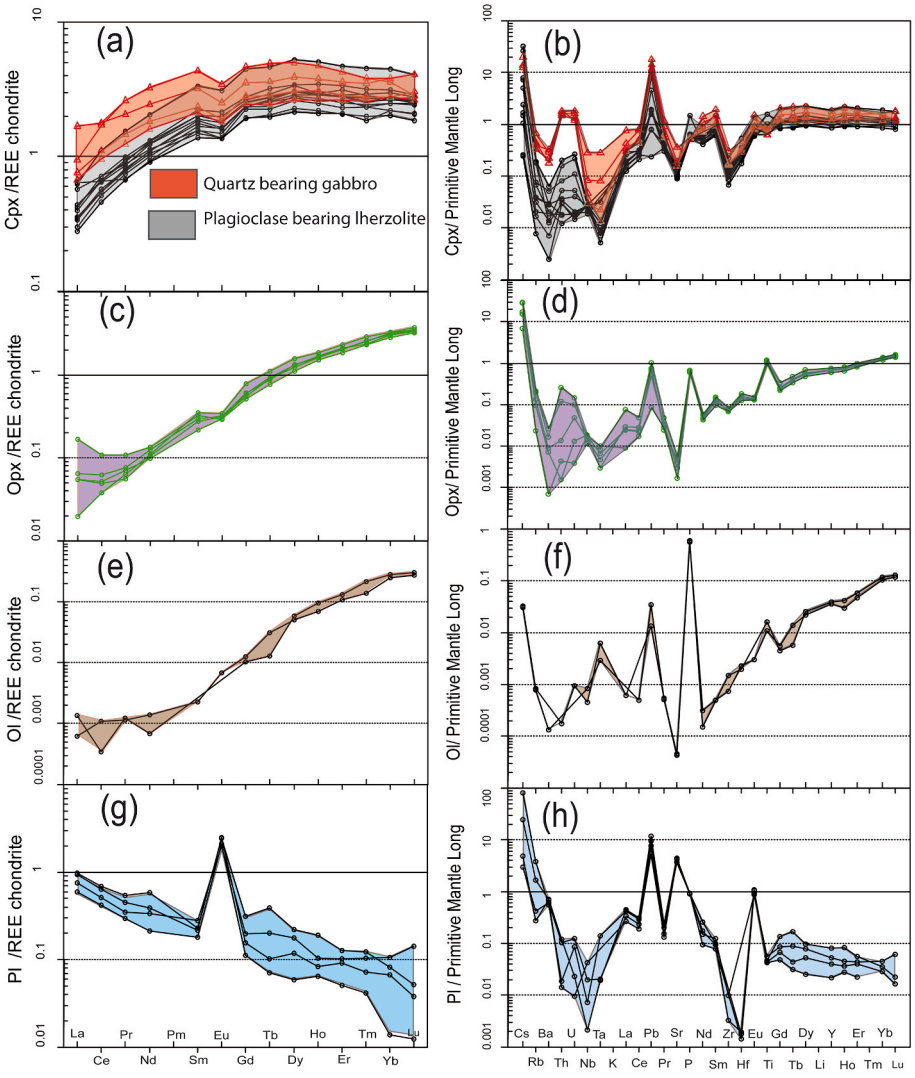

Fig. 6. Chondrite-normalized rare earth element diagrams (normalization after Boynton, 1984) and Primitive Mantle normalized extended trace element diagrams (normalization after Sun and McDonough, 1989)for clinopyroxene (a), orthopyroxene (b), olivine (c) and plagioclase (d) from mafic and ultramafic rocks of the Yaddene Complex.

orthopyroxene, clinopyroxene, plagioclase, and amphibole are reported in Table 1.

- ***Chromian Spinel***

Cr-Spinel (chromite) is an accessory phase in plagioclase-bearing lherzolites (CB34 and CB38). It shows high Cr_2O_3 (42.46–49.68 wt%), and FeO^t (25.8–31.3 wt%) contents relative to MgO (7.19–8.33 wt%). The TiO_2 and Al_2O_3 contents range from 0.25 to 1.92 and from 12.42 to 13.6 wt%, respectively (Table 1).

- ***Olivine***

Olivine was analyzed from the plagioclase-bearing lherzolites CB34 and CB38 (Table 1). It is compositionally homogeneous in both the samples and show $Fo^{86\text{-}88}$ in composition. The NiO, Cr_2O_3, and MnO contents range from 0.24 to 0.29, from 0.01 to 0.05, and from 0.16 to 0.20 wt%, respectively.

- ***Pyroxenes***

Pyroxenes from the plagioclase-bearing lherzolites (CB34 and CB38) were analyzed. Structural formulae of the pyroxenes were calculated based on six oxygen atoms (Table 1).

- ***Clinopyroxene***

The analyzed clinopyroxenes were less homogeneous than orthopyroxenes. They overlap the augite-diopside compositions (Morimoto, 1988) (Fig. 4a) with 21.1–22.9 wt% CaO. They show high #Mg (Mg/Mg + Fe) values (0.89–0.92), relatively high Cr_2O_3 (1.03 wt%) and low Na_2O, K_2O and TiO_2 contents (0.06–0.18, <0.0034 wt%, and 0.13–0.34 wt% respectively).

- ***Orthopyroxene.***

The analyzed orthopyroxene is homogeneous with very high Mg content (#Mg = 0.86–0.87). The Cr_2O_3 contents are higher (0.59 wt%) than that of the clinopyroxene, while the NiO contents are low (0.04–0.09 wt%). The orthopyroxene is compositionally enstatitic ($En_{86–87}$) (Fig. 4b).

- ***Plagioclase***

Table 3
Laser ablation ICP-MS isotopic data for zircons and sphene from the quartz-bearing gabbro CB36 and from the plagioclase-bearing lherzolite CB38 of the Yaddene Complex (Lesser Kabylia, NE Algeria).

Sample	Pb*	Th	U	Th/	208Pb/	207Pb/	±	207Pb/	±	206Pb/	±	Rho	Apparent ages			
	(ppm)	(ppm)	(ppm)	U	206 Pb	206 Pb	(1s)	235U	(1s)	238U	(1s)		206Pb/ 238U	± (1s)	207Pb/ 206 Pb	± (1s)
CB36 quartz-bearing gabbro																
Zircon																
sa_1	37.7	10938	8458	1.29	0.781	0.0483	0.0006	0.0197	0.0003	0.00295	0.00002	0.51	18.99	0.13	115	27
sa_2	33.4	11457	7631	1.50	0.683	0.0624	0.0008	0.0261	0.0004	0.00304	0.00003	0.63	19.57	0.19	686	26
sa_3	40.6	12802	8220	1.56	0.954	0.0573	0.0006	0.0235	0.0003	0.00297	0.00002	0.53	19.12	0.13	504	24
sa_5	7.3	2746	1752	1.57	0.547	0.0464	0.0010	0.0190	0.0005	0.00297	0.00004	0.53	19.12	0.26	16	51
sa_6	9.5	3638	2255	1.61	0.575	0.0728	0.0017	0.0308	0.0009	0.00307	0.00006	0.65	19.76	0.39	1008	46
sa_7	14.6	6967	3175	2.19	0.774	0.0570	0.0010	0.0238	0.0005	0.00303	0.00004	0.59	19.50	0.26	492	39
sa_8	16.7	9115	3813	2.39	0.808	0.0485	0.0008	0.0197	0.0004	0.00295	0.00003	0.53	18.99	0.19	124	38
sa_9	10.3	4170	2320	1.80	0.628	0.0583	0.0013	0.0244	0.0007	0.00303	0.00005	0.59	19.50	0.32	541	48
sa_10	15.7	8351	3507	2.38	0.817	0.0622	0.0010	0.0256	0.0005	0.00298	0.00003	0.54	19.18	0.19	682	33
sh_9	8.3	2639	2128	1.24	0.455	0.0803	0.0019	0.0340	0.0010	0.00307	0.00006	0.63	19.76	0.39	1204	46
Titanite																
sb_0	4.9	1.65	1.64	1.01	2.163	0.8399	0.0266	107.3516	5.1184	0.9270	0.0330	0.75	–	–	–	–
sb_0b	2.9	0.30	0.86	0.34	2.048	0.8196	0.0311	111.4273	6.3335	0.9860	0.0418	0.75	–	–	–	–
sb_1	1.8	0.14	1.45	0.10	1.329	0.8332	0.0251	60.7903	2.5957	0.5292	0.0160	0.71	–	–	–	–
sb_2	4.4	0.34	2.99	0.11	1.336	0.8432	0.0172	88.0582	2.6278	0.7574	0.0165	0.73	–	–	–	–
sb_3	6.0	0.50	3.98	0.13	1.321	0.8445	0.0155	71.6198	1.8836	0.6151	0.0116	0.72	–	–	–	–
sb_4	3.9	0.35	3.30	0.11	1.301	0.8235	0.0165	60.5872	1.7146	0.5336	0.0107	0.71	–	–	–	–
sb_5	3.2	0.38	2.99	0.13	1.323	0.8293	0.0260	37.4406	1.6187	0.3275	0.0097	0.69	–	–	–	–
sb_6	3.0	0.40	2.84	0.14	1.299	0.8301	0.0194	49.3012	1.6104	0.4307	0.0098	0.70	–	–	–	–
sb_7	4.2	0.36	2.43	0.15	1.313	0.8327	0.0230	50.6658	1.9570	0.4413	0.0119	0.70	–	–	–	–
sb_8	4.2	0.36	2.43	0.15	1.313	0.8432	0.0883	110.8450	17.9335	0.9534	0.1176	0.76	–	–	–	–
sb_9	6.5	0.34	2.49	0.14	1.287	0.7677	0.0144	103.3473	2.8947	0.9764	0.0203	0.74	–	–	–	–
sb_10	2.1	0.52	4.25	0.12	1.286	0.8090	0.0230	23.2415	0.8896	0.2084	0.0053	0.67	–	–	–	–
sb_11	2.1	0.33	2.36	0.14	1.299	0.8376	0.0265	34.0868	1.4782	0.2951	0.0088	0.68	–	–	–	–
sb_12	1.8	0.20	1.33	0.15	1.320	0.8240	0.0262	62.2494	2.8049	0.5479	0.0175	0.71	–	–	–	–
sb_13	2.6	0.12	0.90	0.13	1.277	0.8125	0.0211	149.2000	6.0877	1.3318	0.0419	0.77	–	–	–	–
sb_14	3.0	0.35	2.43	0.15	1.301	0.8298	0.0201	56.2103	1.9134	0.4913	0.0118	0.70	–	–	–	–
sb_15	3.6	0.40	2.57	0.15	1.350	0.8337	0.0179	64.9888	1.9794	0.5654	0.0122	0.71	–	–	–	–
sb_16	1.4	0.05	0.30	0.17	1.330	0.8426	0.0344	198.1551	13.3734	1.7055	0.0917	0.80	–	–	–	–
sb_17	1.5	0.01	0.19	0.06	1.342	0.8232	0.0298	527.7401	40.1190	4.6499	0.3109	0.88	–	–	–	–
sb_18	12.0	0.05	0.23	0.20	1.305	0.8307	0.0121	1906.6904	88.9567	16.6468	0.7376	0.95	–	–	–	–
sb_19	4.3	0.03	0.32	0.10	1.335	0.8423	0.0171	721.3088	33.0452	6.2109	0.2552	0.90	–	–	–	–
sb_20	10.7	0.11	1.16	0.09	1.341	0.8324	0.0105	565.2182	14.0714	4.9250	0.1056	0.86	–	–	–	–
sb_21	1.4	0.06	2.11	0.03	1.330	0.8576	0.0363	30.8406	1.7797	0.2608	0.0102	0.68	–	–	–	–
sb_22	1.9	0.30	0.18	1.65	1.315	0.8413	0.0326	449.1353	34.7592	3.8718	0.2594	0.87	–	–	–	–
sb_23	0.7	0.02	0.53	0.04	1.379	0.8554	0.0535	52.0959	4.5240	0.4417	0.0266	0.69	–	–	–	–
sb_24	2.2	0.04	0.49	0.09	1.352	0.8229	0.0341	175.4958	11.7022	1.5468	0.0809	0.78	–	–	–	–
sb_25	2.9	0.25	2.62	0.10	1.345	0.8333	0.0226	47.5788	1.7811	0.4141	0.0107	0.69	–	–	–	–
CB38 plagioclase bearing lherzolite																
Zircon																
sh_1	12.2	4320	3116	1.39	0.444	0.0525	0.0015	0.0219	0.0008	0.00302	0.00006	0.57	19.44	0.39	306	64
sh_2	12.9	4725	3401	1.39	0.467	0.0592	0.0013	0.0244	0.0007	0.00299	0.00005	0.60	19.25	0.32	573	48
sh_3	19.4	6933	4662	1.49	0.479	0.0517	0.0015	0.0214	0.0008	0.00301	0.00006	0.57	19.37	0.39	270	65
sh_4	21.2	6849	5356	1.28	0.428	0.0574	0.0013	0.0241	0.0007	0.00304	0.00005	0.57	19.57	0.32	508	51
sh_5	12.6	4014	3408	1.18	0.393	0.0527	0.0012	0.0216	0.0006	0.00297	0.00005	0.58	19.12	0.32	315	52
sh_7	4.4	948	979	0.97	0.454	0.0556	0.0011	0.0236	0.0005	0.00308	0.00004	0.56	19.82	0.26	435	43
sh_8	22.9	8475	5835	1.45	0.461	0.0596	0.0011	0.0247	0.0006	0.00300	0.00004	0.57	19.31	0.26	590	41
sh_6	16.7	5479	4504	1.22	0.392	0.0856	0.0024	0.0385	0.0014	0.00326	0.00008	0.65	21.01	0.51	1329	54

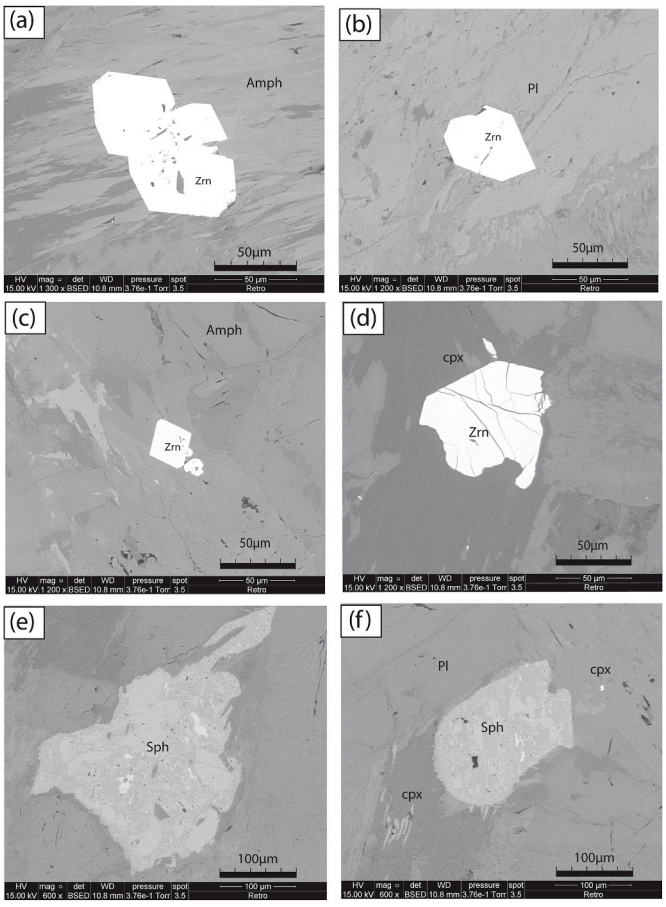

Fig. 7. Scanning Electron Microscope (back-scattered electron mode) images of zircon from the quartz-bearing gabbro CB36 (a), (b) & (c) and from the plagioclase-bearing lherzolite CB38 (d). Sphene (c) & (d) are from the quartz-bearing gabbro CB36.

Plagioclase minerals in the quartz-bearing gabbro (CB36; Table 1) show homogeneous anorthitic composition ($An_{93–95}Ab_{06–05}Or_0$) which reflects a magmatic origin, where the plagioclase did not undergo any albitization processes.

- ***Amphibole***

The structural formulae of amphibole from quartz-bearing gabbro and plagioclase-bearing lherzolite, were calculated based on 23 oxygen atoms. Secondary amphibole in quartz-bearing gabbro (CB36) is calcic amphibole with CaB ≥1.50, (Na + K)A ≤ 0.50, CaA ≤0.50, and, 0.67 ≤ #Mg ≤ 0.82. Primary amphibole in the plagioclase-bearing lherzolite (CB34) show a composition with CaB ≥1.50, (Na + K)A ≥ 0.50, Ti < 0.50, and #Mg (0.85–0.86). Using the classification of Hawthorne et al. (2012), secondary amphibole from the quartz-bearing gabbro plots mainly in the tremolite field, while primary amphibole from plagioclase-bearing lherzolite is classified as pargasite (Fig. 5).

5.2. *Trace elements chemistry of minerals*

"In situ" trace element compositions of the minerals are reported in Table 2. Rare earth element patterns (REE) of the analyzed minerals have been normalized to chondrite (Boynton, 1984), whereas multiel-ement patterns have been normalized to primitive mantle (Sun and McDonough, 1989).

- Clinopyroxene

Clinopyroxenes from the quartz-bearing gabbro (CB36) and plagioclase-bearing lherzolites (CB34 and CB38) show similar patterns for primitive mantle-normalized incompatible elements and chondrite-normalized REE (Fig. 6a and b). They are depleted in light (L) REE ($La/Sm_N = 0.18–0.52$) and heavy (H) REE relative to medium (M) REE ($Sm/Yb_N = 0.52–1.21$) as in normal mid-oceanic ridge basalt (N-MORB). They show a negative Eu anomaly ($Eu/Eu^* = 0.13–0.86$) suggesting that their crystallization occurred either after plagioclase or from melts that have been fractionated by plagioclase accumulation or removal. In the primitive mantle-normalized diagrams, all clinopyroxenes exhibit enrichment in large ion lithophile elements (LILE), notably Cs and Rb. High-field strength elements (HFSE) (Zr, Hf, Nb, and Ta) show signifi-cant (Hf, Zr and Ti) to weak (Nb-Ta) negative anomalies. The negative Sr anomaly is consistent with the negative Eu anomaly corresponding to plagioclase fractionation. Most of the analyzed crystals display a pro-nounced positive Pb anomaly.

- Orthopyroxene.

Orthopyroxenes from plagioclase-bearing lherzolites (CB34 and CB38) were analyzed (Fig. 6c and d). They display low total REE con-tents ranging from 2.28 to 3.44 ppm. In the chondrite-normalized dia-grams, they show depleted LREE patterns ($(La/Sm)_N = 0.02–0.52$), and negative Eu anomalies ($Eu/Eu^* = 0.02–0.76$). In the primitive mantle-normalized diagrams, they exhibit a LILE enrichment (up to 10 times the primitive mantle) and weak-to-moderate negative Ta, Hf, Zr and Ti anomalies. Similar to clinopyroxenes, the orthopyroxenes display negative Sr anomalies, which is consistent with negative Eu anomalies, and large positive Pb spikes.

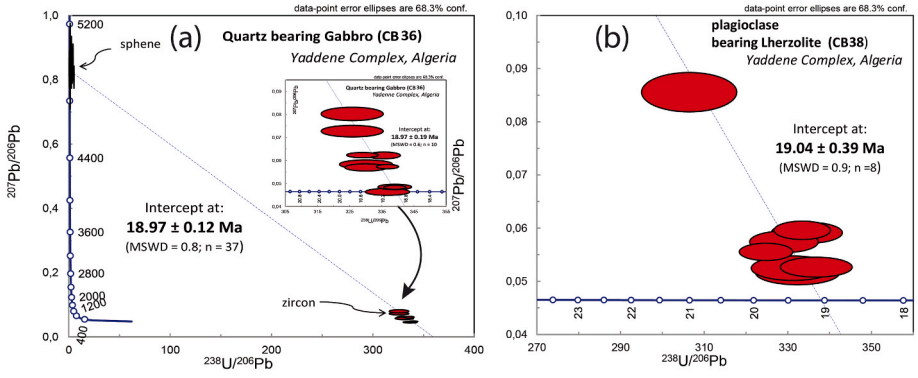

Fig. 8. Tera-Wasserburg concordia diagram for: (a) zircon and sphene from the quartz-bearing gabbro CB36 and, (b) zircon from the plagioclase-bearing lherzo-lite CB38.

Table 4
Major and trace elements analyses of selected mafic and ultramafic rocks form Yadenne complex. LOI: loss of ignition. #Mg = /(Mg + Fe), (data after Abbassene et al., 2016).

Sample name	CB 34	CB 38	CB 39	CB 36
Major elements (wt%)				
SiO2	42.67	41.35	49.43	51.47
TiO2	0.17	0.16	0.18	0.34
Al2O3	5.36	5.13	18.67	17.09
Fe2O3 (t)	9.26	8.93	5.53	6.47
MnO	0.14	0.14	0.13	0.12
MgO	34.88	33.15	10.78	9.27
CaO	3.77	3.77	13.32	12.55
Na2O	0.15	0.16	0.73	0.71
K2O	0.06	0.06	0.06	0.17
P2O5	0.03	0.03	0.01	0.02
L.O.I	7.82	6.22	2.12	3.38
Total	104.31	99.09	100.96	101.59
Mg#	88.19	88.04	79.44	73.95
Trace elements (ppm)				
Cs	1.94	1.07	1.47	2.38
Rb	3.24	2.91	2.88	8.57
Ba	6.55	6.39	5.95	10.63
Sr	11.89	16.43	71.91	86.13
Pb	0.81	0.92	0.71	2.77
Th	0.30	0.26	0.25	0.57
U	0.07	0.05	0.05	0.09
Zr	7.99	7.04	6.02	10.45
Hf	0.32	0.29	0.25	0.47
Ta	0.04	0.03	0.04	0.09
Y	5.46	5.07	5.67	11.98
Nb	0.55	0.50	0.54	1.43
Sc	15.63	16.16	35.04	36.57
Cr	bdl	1427	bdl	345.7
Ni	bdl	1248	bdl	82.86
Co	89.09	90.62	27.04	23.79
V	91.13	89.08	143.12	168.66
Ga	4.35	4.24	11.08	11.71
Zn	47.90	44.21	33.73	30.20
Cu	25.06	28.61	0.40	5.74
La	1.09	1.00	1.00	2.32
Ce	2.42	2.30	2.29	5.21
Pr	0.33	0.31	0.31	0.70
Nd	1.53	1.42	1.47	3.20
Sm	0.48	0.45	0.48	0.99
Eu	0.17	0.16	0.23	0.47
Gd	0.67	0.63	0.68	1.35
Tb	0.13	0.12	0.13	0.25
Dy	0.84	0.79	0.90	1.64
Ho	0.19	0.18	0.20	0.36
Er	0.57	0.53	0.59	1.07
Yb	0.56	0.52	0.58	1.02
Lu	0.09	0.08	0.09	0.16

- Olivine

Olivine from the plagioclase bearing lherzolite (CB34) (Fig. 6e and f) shows very low REE concentrations (total REE contents of 0.12–0.13). In the chondrite-normalized diagrams, they are characterized by LREE-depleted patterns with $(La/Yb)_N$ = ~0 and no Eu anomalies. In the primitive mantle-normalized patterns, they display a negative Sr anomaly, positive Pb spike, and significant LILE enrichment (Cs), but slight enrichment of Rb compared to the orthopyroxene pattern. A positive Ta anomaly, weak negative Nb and Ti anomalies and a positive U anomaly are also observed in the mantle-normalized patterns.

- ***Plagioclase***

The plagioclase crystals analyzed from quartz-bearing gabbro (CB36 and CB39) (Fig. 6g and h) are characterized by low REE contents compared to chondrite. They display LREE enriched patterns (La/Yb_N = 7.17–13.91) and pronounced positive Eu anomalies (Eu/Eu* = 8.56–13.69) in the chondrite-normalized diagram (Fig. 6g). The primitive mantle-normalized diagram (Fig. 6h) shows LILE enrichment (Cs, Rb, and Ba), positive Sr and Pb anomalies and negative HFSE anomalies (Nb, Ta, and Zr-Hf).

5.3. *Geochronology*

LA-ICP-MS in situ U-Pb analyses of zircon and titanite from quartz-bearing gabbro (CB36) and zircon from plagioclase-bearing lherzolite (CB38) were performed on polished thin sections (Table 3). Crystals were examined by scanning electron microscopy (SEM) before analysis (Fig. 7). Three zircons were detected from sample CB36 and two from CB38.

The zircons from sample CB36 are euhedral with sharp terminations (Fig. 7a–c), suggesting a magmatic origin. The largest grain was c. 110 μm long and 50 μm wide, containing small inclusions, mainly in its center. The analyzed crystals are rich in U and Th (1750–8500 ppm and 2600–12800 ppm, respectively), resulting in high Th/U ratios (1.2–2.4) (Table 3). Such high U and Th concentrations are unusual but can be found in zircons from gabbroic rocks (e.g., Stern et al., 2020), and suggest that the analyzed zircons crystallized from a differentiated gabbroic magma. Zircon analyses define an age of 18.97 ± 0.19 Ma (MSWD = 0.6; n = 10) in the Tera-Wasserburg concordia diagram (Fig. 8a). Titanite crystals are irregular in shape (Fig. 7e and f) with complex internal structures. Analyses performed on different domains were characterized by low U contents (<5 ppm) and consequently low radiogenic Pb. Furthermore, in the Tera-Wasserburg diagram, the data points showed a small spread (Fig. 8a). Owing to these features, age calculation was not possible from titanite alone. However, their location close to the upper intercept was used to define the common Pb component without making any inferences on its isotopic composition. Thus, the entire dataset (zircon + titanite) provides an age of 18.97 ± 0.12 Ma (2σ, MSWD = 0.8, n = 37), which we attribute to the crystallization age of zircon in the gabbroic magma.

The two grains from sample CB38 were partly euhedral with euhedral terminations on one side (left part of the grain in Fig. 7d), but with a complex curvilinear shape in other parts, suggesting a late crystallization stage close to sub-solidus conditions or corrosion by fluids of initially euhedral grains. The grains display very high U (1000–6000 ppm) and Th (1000–8500 ppm) contents consistent with a late crystallization. Eight spots were performed on the two grains and showed a chord in the Tera-Wasserburg concordia diagram, providing an age of 19.05 ± 0.39 Ma (MSWD = 0.9, n = 8) (Fig. 8b). Zircon normally does not form in a primary peridotite mineral assemblage because the activity of Zr and Si in ultramafic rocks is too low (Palme and O'Neill, 2003). However, zircon-bearing orogenic peridotites are occasionally reported and the origin of zircon is often ascribed to metamorphism and/or local metasomatism of the host peridotite during subduction-related fluid/-melt processes (e.g. Tumiati et al., 2007; Marocchi et al., 2009). It is striking to note that this age is identical to the magmatic crystallization age of zircon from the quartz-bearing gabbro CB36 and we thus attribute zircon growth in the lherzolite to metamorphic/metasomatic processes related to emplacement of the gabbroic magma.

5.4. *Whole rocks geochemistry*

The thin sections (samples CB 34, CB 38, CB36 and CB39) studied and analyzed in this study, were taken from the same samples analyzed by Abbassene et al. (2016). To support our arguments on the genesis of the mafic and ultramafic rocks of the Yaddene complex and to further support our geodynamic model we have added these whole rock data (See Table 4).

Their chemical composition shows very high MgO contents for plagioclase-bearing lherzolite (33.15–34.88 wt%) and high MgO contents for quartz-bearing gabbro (9.27–10.78 wt%). The CaO contents is high and ranges from 3.77 to 13.32 wt% for mafic and ultramafic rocks. However, the K_2O, Na_2O and TiO_2 contents are very low and range from

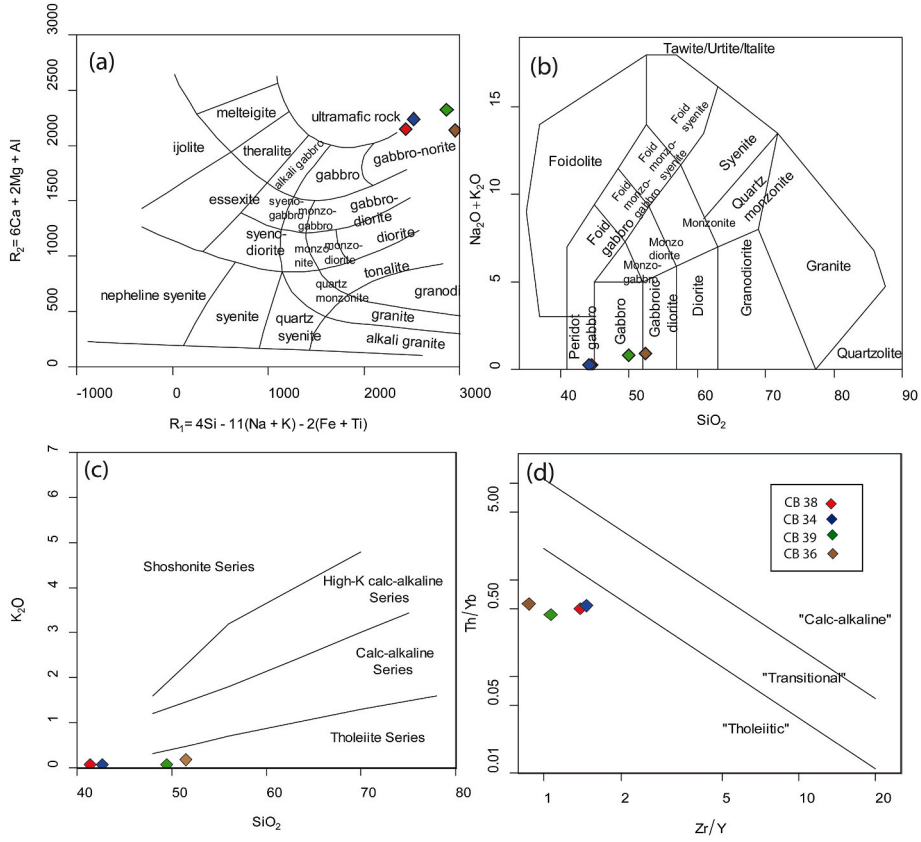

Fig. 9. TAS ($Na_2O + K_2O$ Vs SiO_2) diagram classification (Middlemost, 1986); **(b)** Binary classification diagrams R1[= 4Si-11(Na + K)-(Fe + Ti)] vs R2[= (6Ca+2 Mg + Al)] (De la Roche et al., 1980) of mafic and ultramafic rocks from Yaddene (CB34 CB38 CB39 CB36); (c) K_2O vs SiO_2 diagram (Peccerillo and Taylor, 1976).(d) (Th/Yb) vs (Zr/Y) diagram (Ross and Bédard, 2009).

0.06 to 0.17 wt%, from 0.15 to 0.73 wt% and from 0.16 to 0.34 wt% respectively. Using the classification diagram R1 [= 4Si-11(Na + K)-(Fe + Ti)] vs R2 [= (6Ca+2 Mg + Al)] (De la Roche et al., 1980), the whole rocks plot in the field of ultramafic rocks and gabbro-norite. When using the TAS diagram ($K_2O + Na_2O$ vs SiO_2) samples CB34 and CB38 plot in the peridotite field, and samples CB39 and CB36 are in the gabbro and dioritic gabbro field. This result reflects the nature of primitive liquid, and confirms the picritic nature of the parental magma (Fig. 9a and b). Their very low K and Na content is consistent with their tholeiitic nature (Fig. 9c and d). Mafic and ultramafic rocks show also very high Ni and Cr contents between 1248-83 ppm and 1427-346 ppm respectively.

6. Discussion

6.1. Petrogenesis

Cumulate (poikilitic and intergranular) textures observed in the mafic and ultramafic rocks of the Yaddene complex can be explained by mineral accumulation during primary magma crystallization.

Octahedral spinel inclusions in the olivine from ultramafic rocks of the Yaddene complex indicate a continuous fractional crystallization of spinel with olivine and other silicate phases (orthopyroxenes and clinopyroxenes) and reflect the early crystallization of spinel compared to other silicate phases at higher temperatures (e.g; Kamenetsky et al., 2001, 1997). The absence of Cr-spinel in the most differentiated magma (quartz-bearing gabbro) indicates that all Cr was used up by spinel during fractional crystallization of plagioclase-bearing lherzolite.

When observing the #Mg values of spinel and olivine from the Yaddene plagioclase-bearing lherzolites, a large difference between these two primitive phases is evidenced. #Mg range from 0.30 to 0.36 and from 0.86 to 0.89 for spinel and olivine respectively, and the distribution coefficient [Kd $^{Sp-Ol}$= $(Mg/Fe)^{Ol}/(Mg/Fe2)^{Sp}$] shows a large difference (11.90–17.09). This difference in #Mg of olivine-spinel pairs is caused by a post-crystallization sub-solidus re-equilibration of these phases at lower temperatures. This re-equilibration depends on the distribution of Mg and Fe between olivine and spinel and the relative activity of Cr and Al in spinel (Dick and Bullen, 1984). In other cases, it can also depends on the substitution of Mg and Al by Fe and Cr (Allan et al., 1988). This sub-solidus re-equilibration of iron and magnesium involves not only olivine and spinel, but also other phases containing spinel such as orthopyroxene or clinopyroxene (Li, 1991).

Magmatic spinels are commonly used to constrain the source of the parental mantle and the degree of partial melting using their #Cr (e.g. Arai, 1992; Bonatti and Michael, 1989; Kamenetsky et al., 2001, 1997). Analyzed spinel plots out of the spinel-olivine mantle array (Fig. 10a), which confirms its magmatic origin, as well as a harzbugitic origin of the parent mantle source.

Although the #Mg of the hosted olivine crystals in the plagioclase-bearing lherzolite are high (0.86–0.89), they remain lower than the #Mg in the mantle olivines (#Mg > 0.90). This is not only confirmed by the #Mg but also by the NiO contents of these olivines (≤0.29%), which are significantly lower than those of the upper mantle olivines (>0.31%). Moreover, microscopic observation shows the absence of "kink-band" or deformation macles. The NiO vs. Fo diagram (Takahashi, 1985) shows that the olivine in the plagioclase-bearing lherzolite is magmatic in origin and plot out of the mantle olivine field (Fig. 10b).

High #Cr in the studied spinel reflects a high degree of partial melting of the mantle source. The #Mg vs #Cr diagram (Fig. 10c) indicates that the studied spinel resulted from accumulation during fractional crystallization of a picritic magma with chemical characteristics akin to those forming stratiform complexes.

Ti undergoes very limited, if any, change during post-emplacement

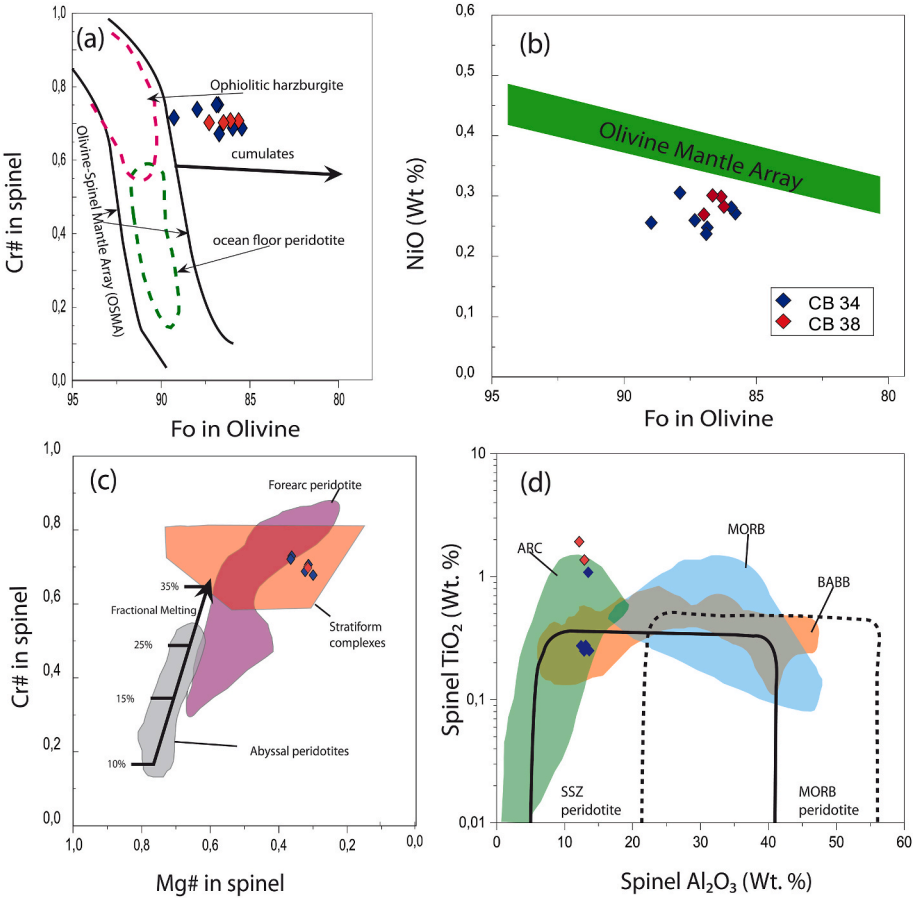

Fig. 10. Discrimination diagrams for spinel-olivine pairs from the plagioclase-bearing lherzolites CB34 and CB38 (a) Cr# in spinel versus Fo in olivine. OSMA (olivine-spinel mantle array) is from Arai (1992); (b) NiO versus Fo in olivine. Olivine Mantle Array (mantle peridotite range) is from Takahashi (1985); (c) Cr# versus #Mg = (Mg/(Mg + Fe)). Fields of abyssal and forearc peridotite stratiform complexes (After: Dick and Bullen, 1984; Hirose and Kawamoto, 1995). percentage of partial melting Arrow (Hirose and Kawamoto, 1995); (d) TiO_2 vs Al_2O_3Tectonic discriminating diagram of spinel forming Lherzolite from: Kamenetsky et al. (2001) SSZ (supra--subduction zone) peridotite; MORB peridotite; mid-ocean ridge basalt (MORB); island-arc basalt (ARC); back-arc basin basalt (BABB).

re-equilibration, due to its low diffusivity within olivine in contrast to Mg-Fe (Scowen et al., 1991). Analyzed spinel shows compositions akin to those from magmas formed in a back-arc basin environment with low Al_2O_3 content (Fig. 10d) and, in the Al_2O_3 vs TiO_2 tectonic discrimination diagram of Kamenetsky et al. (2001) they plot near the field of arc environments.

Clinopyroxenes from plagioclase-bearing lherzolites show high SiO_2 and relatively low Al_2O_3 contents with a sub-alkaline composition (Fig. 11a) reflecting the tholeiitic affinity of the host magma (Le Bas, 1962).

Microscopic observations of the pyroxenes in thin sections show the coexistence of orthopyroxene and clinopyroxene alongside and sharing the same rims, without any exsolution lamellae. In addition the almost identical #Mg in both pyroxenes excludes the existence of a sub-solidus re-equilibration, but a solidus equilibrium during a continuous crystallization. The presence of olivine included in pyroxenes and #Mg positively correlated between olivine and pyroxenes also confirm the continuous fractional crystallization with olivine crystallized well before pyroxenes without any post-crystallization (Fe-Mg) chemical exchange.

Ti, Cr, and Ca contents in clinopyroxene can be used to pinpoint the geodynamic settings from which the magmas originate (Beccaluva et al., 1989a,b; Leterrier et al., 1982). In the plagioclase-bearing lherzolite, the analyzed clinopyroxene shows an intermediate composition between magmas from non-orogenic environments (high Ti + Cr contents) and boninitic magmas from island arc environments (low Ti + Cr contents) (Fig. 11b). The TiO_2 content of clinopyroxene in plagioclase-bearing lherzolite ranges from 0.14 to 0.32 wt% indicating Ti depletion of the host magma. Therefore, it confirms that Yaddene rocks crystallized from a low-titanium parent magma, which is consistent with a subduction zone environment (e.g; Green et al., 2006; Pearce and Norry, 1979; Tribuzio et al., 2008).

Tectonic discrimination diagrams (Beccaluva et al., 1989a,b) using the distribution of SiO_2, Al_2O_3, and TiO_2 in clinopyroxene allows a distinct classification of magma types. The clinopyroxene from the plagioclase-bearing lherzolite shows high SiO_2 and very low Na_2O and TiO_2 contents, which is typical of clinopyroxene from subduction zone magmas (IAT, BABB, and Boninite). In addition all data points, but one, plot in the BABB field (Fig. 11c).

Under a transmitted light microscope, amphibole shares its borders with pyroxenes. It displays almost similar #Mg and a high CaO content, similar to that observed for the clinopyroxene. This is taken as evidence that these amphiboles are from the same source and represent the last crystallized phase in the ultramafic rocks. The higher Al_2O_3 component compared to other silicate phases is per continuous crystallization chain, and Al_2O_3 was not fractionated by other silicate phases until the amphibole crystallization.

Amphibole (pargasite) in the plagioclase-bearing lherzolite incorporates a fluid-rich component from the subducted plate. This information is taken as evidence that the magmas have a proximal position relative to the island arc and that they crossed the metasomatized mantle enriched in fluids from the subducted plate below.

The CIPW normative calculation (Table 5) shows the presence of oversaturated silica in mafic magmas expressed by the presence of normative quartz (1.8 and 7.1%). These results confirm that the interstitial quartz observed in mafic rocks is a primary quartz filling the last voids between the crystals at the end of fractional crystallization.

The tectonic setting of the Yaddene ultramafic and mafic rocks can be investigated using various tectonic discriminatione diagrams. In the Y/15-La/10-Nb/8 ternary diagram (Cabanis and Lecolle, 1989) these rocks show a BABB composition (Fig. 12a) and in the V-Ti diagram (Fig. 12b) (Shervais, 1982) they plot in the field of IAT or proximal BABB. Using

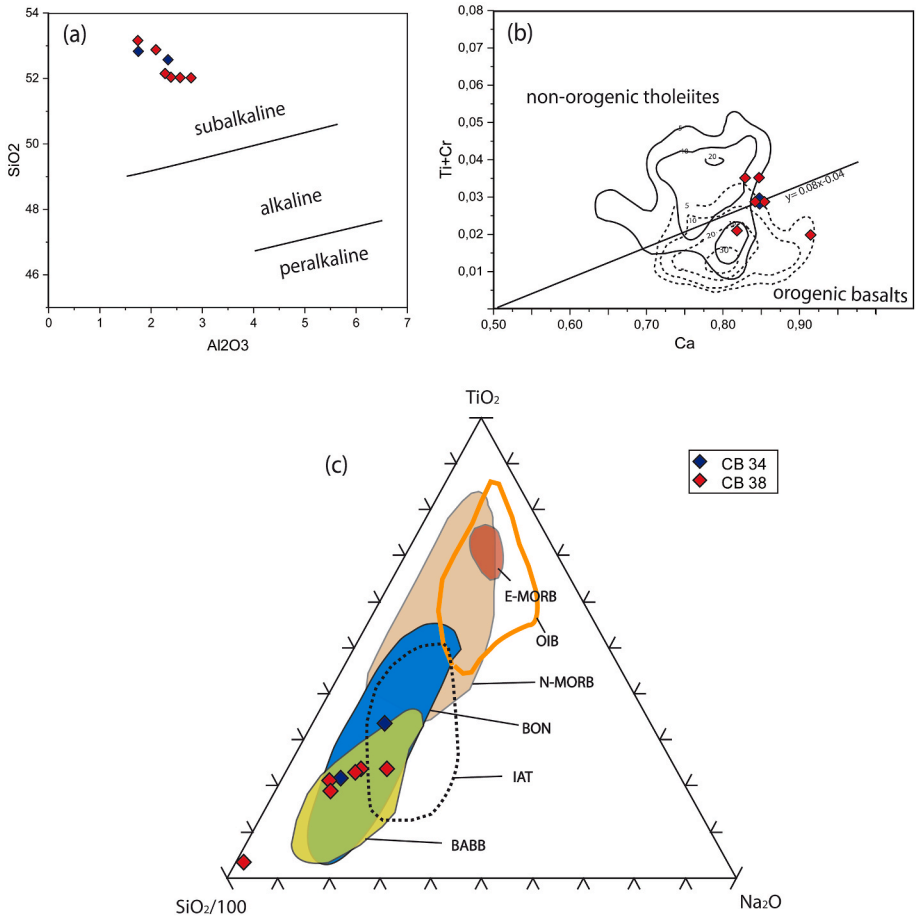

Fig. 11. Discrimination diagrams for clinopyroxene analyses from the plagioclase-bearing lherzolites CB34 and CB38. (a) SiO_2 vs. Al_2O_3 binary diagram for pyroxene (after Le Bas, 1962) (b) Ti + Cr versus Ca diagram (Leterrier et al., 1982); (c, d, e) tectonic discrimination diagrams (c) TiO_2 - $SiO_2/100$ - Na_2O (wt%) discrimination diagram (Beccaluva et al., 1989a,b) for clinopyroxene from ultramafic rocks of the Yaddene layered complex. E-MORB: enriched mid-ocean ridge basalt; N-MORB: normal mid-ocean ridge basalt; OIB: ocean island basalt; BON: boninite; IAT: island-arc tholeiite; BABB: back-arc basin basalt.

Table 5
CIPW normative calculation of mafic and ultramafic rocks from Yaddene complex. Q: Quartz; Or: Orthoclase; Ab: Albite; An: Anorthite; Di: Diopside; Hy: Hypersthene; Ol: Olivine; Mt: Magnetite; Il: Ilmenite; Ap: Apatite.

	CB38	CB34	CB39	CB36
Q	0.000	0.000	1.811	7.155
Or	0.355	0.355	0.355	1.005
Ab	1.354	1.269	6.177	6.008
An	13.102	13.775	47.489	42.943
Di	4.268	3.737	14.712	15.328
Hy	18.415	18.026	25.506	22.422
Ol	52.620	56.529	0.000	0.000
Mt	2.407	2.422	2.436	2.668
Il	0.304	0.323	0.342	0.646
Ap	0.071	0.071	0.024	0.047
Sum	92.896	96.506	98.851	98.221

the Th/Yb-Nb/Yb diagram after (Pearce, 2008) (Fig. 12c) it can be seen that the Yadenne rocks plot above the mantle array, between the N- and E-MORB, and between the two domains of back-arc basin basalt & arc rift basalts (see data from Pearce, 2008; Pearce et al., 2005).

The chondrites normalized Rare-earth elements (REE) patterns (Fig. 13a) of mafic/ultramafic rocks show similar trends although the quartz–bearing gabbro CB36 is more enriched. All patterns are LREE enriched with $La/Yb)_N$ between 1.16 and 1.53 and display flat HREE patterns with $Gd/Yb)_N$ ranging 0.96–1.06. The patterns of the ultramafic rocks are characterized by a slight negative Eu anomaly, while mafic rocks display a marked positive Eu anomaly attributed to plagioclase accumulation. The very low LREE contents of minerals (clinopyroxenes, orthopyroxene and olivine) in the plagioclase lherzolites contrast with the LREE enriched patterns of the whole rock samples. Since minerals were analyzed in situ by laser ablation, LREE enrichment in the WR samples is likely attributed to secondary alteration or metasomatic processes occurring after olivine/pyroxene crystallization. In any case, in-situ analyses substantiate that the mantle source of the parental magmas was depleted in LREE (harzburgitic source).

Primitive mantle normalized multi-element diagrams (Fig. 13b) show a similar trend for all patterns. They show enrichments in LILE (K, Rb, Ba), negative Nb-Ta anomalies and marked Pb spikes. These patterns are broadly similar to what is observed for in-situ analyses of minerals, notably for clinopyroxene (see Fig. 6). These characteristics (LILE enrichments, Pb spikes and Nb-Ta negative anomalies) are typical of subduction related environments with LILE and Pb enrichments related to slab-derived fluids, and HFSE (Nb-Ta, Zr-Hf & Ti) depletion to retention in the slab (Pearce, 1982; Perfit et al., 1980).

Analyses performed on minerals have been used to calculate the T and P registered by the different types of minerals. When using thermometers or barometers, it is essential to investigate the equilibrium between the different phases, otherwise the calculated P-T conditions can be meaningless. To check the reliability of our thermobarometric results, we have calculated the KD of (Fe-Mg) exchanges between the used mineral pairs.

KD of olivine, and whole rock composition based on Fe-Mg exchange between both phases ranges from 0.44 to 0.54. This ratio is slightly higher than experimental data of Roeder and Emslie (1970) which is almost constant at 0.30 ± 0.03. Our result remains however acceptable, because KD $(Fe\text{-}Mg)^{ol\text{-}liq}$ decreases with decreasing of SiO2 (Gee and Sack, 1988), and increases with increasing Pressure (Herzberg and O'Hara, 1998; Putirka, 2005). It is noteworthy that even the results measured by Putirka (2008) are in the range 0.20–0.56, thus giving

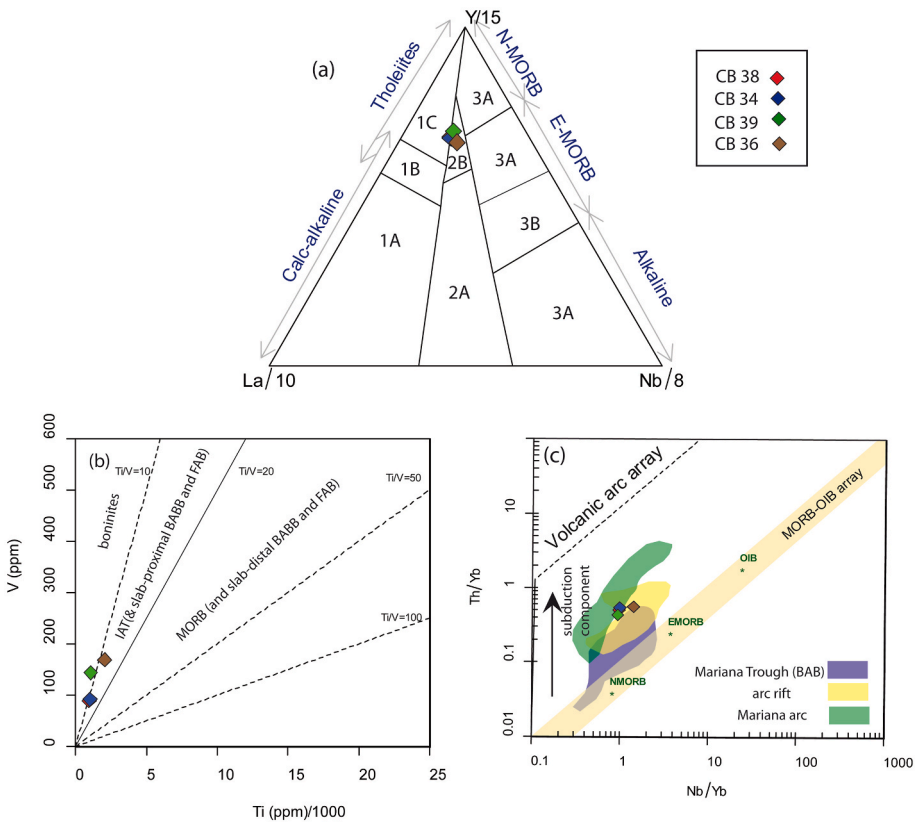

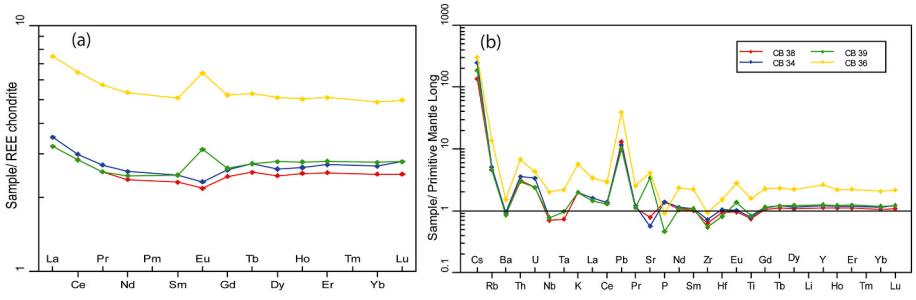

Fig. 12. (a) Y/15-La/10-Nb/8 diagram after: Cabanis and Lecolle (1989). 1, Volcanic arc basalts: 1A, calc-alkaline basalts; 1B, overlap between 1A and 1C; 1C, volcanic arc tholeiites. 2, Continental basalts: 2A, continental basalts; 2B, back-arc basalts. 3, Oceanic basalts: 3A, alkaline basalts; 3B, C, EMORB; 3D, N-MORB; (b) V vs Ti diagram (Shervais, 1982 and modified after Pearce, 2014); (c) Th/Yb–Nb/Yb diagram after: Pearce (2008): datas from Mariana arc, arc rift & back arc basin from:Pearce et al. (2005).

Fig. 13. Chondrite-normalized rare earth element diagrams (normalization after Boynton, 1984) and Primitive Mantle normalized extended trace element diagrams (normalization after (Sun and McDonough, 1989) for plagioclase-bearing lherzolite (CB34,CB38) and quartz-bearing gabbro(CB39, CB36).

support to our thermometric results.

For clinopyroxene and orthopyroxene, the calculated $KD^{opx\text{-}cpx}$ range from 0.72 to 0.84. The best experimental tests of Putirka (2008) provide a mean KD value of 1.09 ± 0.14, but in calculations used by Putirka (2008), KD for pyroxene pairs range from 0.597 to 1.2, which shows that small variations are acceptable when calculating P-T conditions. To confirm our result we used the method of Brey and Köhler (1990), already tested by these authors on ultramafic rocks and gabbros. The only condition in this method is that #Mg Opx and #Mg Cpx >0.75. Even the method of Wells (1977) shows similar results and confirms that our test on pyroxene pairs is reliable.

For plagioclase the calculated KDs range from 0.23 to 0.30, which is very similar to the experimental data of Putirka (2008) where the $KD^{pl\text{-}liq} = 0.27 \pm 0.18$.

Given that the partition coefficient calculated are in agreement with equilibrium conditions, we then calculated the crystallization temperatures for all the mineral analyzed.

The crystallization temperature of olivine from the ultramafic unit of Yaddene was calculated from its mineral chemistry (this study) and whole-rock composition (Abbassene et al., 2016). Using the methods of Sisson and Grove (1993a, 1993b) and Putirka (2008) (Eq. 22 and Eq. 21 in RiMG) (see Table 6), we respectively obtain the following crystallization temperatures: 1231–1245, 1248–1262 and 1240–1249 °C.

Plagioclase is part of the continuous series during fractional crystallization of basic magmas, and their crystallization temperatures provide information on their formation conditions. Using the thermometers of Putirka (2005) (Eq. 23) and Putirka (2008) (Eq. 24a and 26), the crystallization temperature of plagioclase was calculated to be 1094–1208, 1092–1190, and 1147–1210 °C (Table 6). These values are lower than the crystallization temperature of olivine (*c.* 1230–1260 °C).

Pyroxene thermometry was performed using the methods of Brey and Köhler (1990), Putirka (2008), and Wells (1977) (Table 6), which yielded temperatures of 858–1065, 931 to 1069, and 929–1110 °C, respectively.

Using the thermometer of Otten (1984) (Table 6), primary amphibole from plagioclase-bearing lherzolite rocks of the Yaddene complex yielded temperatures of 611–777 °C, which are significantly lower than those obtained for other minerals (olivine, plagioclase and pyroxene).

Table 6
Thermobarometric calculations for minerals in the mafic/ultramafic rocks of the Yaddene massif. Temperatures calculated for: Olivine; Plagioclase; Pyroxene and Amphibole (pargasite). Olivine, pyroxene and amphibole are from the plagioclase-bearing lherzolites CB34 and CB38. Plagioclase are from the quartz-bearing gabbro CB36. Pressures calculated for pyroxene from lherzolites CB34 and CB38.

sample	couple	Putirka et al. (2007)		Putirka et al.		Observed
		Their Eqn. 4		Their Eqn. (2)	Sisson & Grove	
		Eqn 22 in RiMG T(C)		Eqn. 21 in RiMG T(C)	(1992) Eqn. 2 T (C)	KD(Fe-Mg)
cb38	Ol-Liq	1261.91		1240.21	1244.50	0.45
		1250.62		1245.79	1232.83	0.51
		1251.16		1246.50	1233.30	0.55
		1249.11		1243.84	1231.53	0.51
		1248.34		1242.84	1230.86	0.48
		1252.89		1248.74	1234.79	0.54
		1249.11		1243.83	1231.53	0.50
cb34		1251.36		1246.75	1233.47	0.53
		1249.92		1244.89	1232.23	0.51
		1250.15		1245.19	1232.43	0.53
		well (1977)	Brey and Kohler 1990 T (BKN)	putrika (2008) RiMG		Observed
				Eqn 36	Eqn 38	
		T(C)	T(C)	T(C)	P(kbar)	KD(Fe-Mg)
cb34	Opx-Cpx	1068.37	1012.99	1031.50	1.98	0.72
		1045.55	1014.66	1030.12	3.31	0.84
		1044.46	1008.90	1015.13	1.78	0.82
cb38		929.01	858.25	931.94	0.93	0.81
		1110.40	1065.30	1063.34	3.38	0.82
		1084.06	1048.69	1069.58	2.90	0.79
		1060.99	1013.88	1052.15	3.32	0.72
		1066.16	1018.35	1023.56	1.15	0.73
		1070.33	1016.39	1043.58	1.49	0.72
		1067.92	1022.09	1060.07	2.67	0.74
		Putirka (2005) Eqn 23		Putirka (2008) Eqn (24a)	Eqn 26	Observed
		T(C)		T(C)	T(C)	KD(Ab-An)
CB36	Pl-Liq	1170.95		1141.74	1175.65	0.28
		1093.68		1092.20	1115.84	0.23
		1170.86		1141.64	1175.65	0.27
		1126.88		1137.28	1159.74	0.25
		1207.74		1189.86	1223.48	0.24
		1117.29		1124.17	1146.92	0.26
		1197.42		1176.21	1209.50	0.30
		1117.38		1124.27	1146.92	0.27
		1171.01		1141.81	1175.66	0.30
		1093.72		1092.23	1115.85	0.24
		Otten (1984) Ti		T(C)		
CB34	Amph	0.14		713.79		
		0.05		611.24		
CB38		0.19		777.32		

This result represents the temperature of the last crystallized phase in the ultramafic rock.

The obtained temperatures are in agreement with the absence of Eu anomalies in olivine (early crystallizing minerals compared to plagioclase) and the presence of such an anomaly in pyroxenes (coeval or late crystallizing minerals compared to plagioclase).

Additionally, pyroxenes from plagioclase-bearing lherzolites (CB34 and CB38) were used to calculate the pressure conditions of emplacement using Eq. 38 of the geobarometer from Putirka (2008), which does not consider the temperature conditions. The obtained pressure estimates of 0.9–3.4 kbars (Table 6) suggest an intrusive depth of 3–10 km, i.e., at an upper-crustal level. The low level of emplacement of the picritic magmas is consistent with an extensional setting, in which magmas reach high crustal levels.

6.2. *Geodynamic implications*

The age and geochemical signatures of mafic/ultramafic rocks from the Yaddene complex help to constrain the geodynamic setting of its emplacement and provide implications for the evolution of the Algerian Basin.

Seismic data along the northern margin of Africa (Arab et al., 2016; Bouyahiaoui et al., 2015) show that the southern margin of the Algerian Basin corresponds to a rifted continental domain, where the *c.* 30 km thick continental crust progressively thins northward and transitions to a *c.* 6 km thick oceanic crust. Therefore, the northern margin of Africa was interpreted as an ocean-continent transition (OCT) zone. Consequently, the onshore OMK series has been attributed to a syn-rift sedimentation, starting with basal fluvial conglomerates and evolving upward to finer sediments (shale) deposited in a marine environment. The detailed relationship between the mafic/ultramafic rocks of the Yaddene complex and the surrounding rocks of the OMK has not been explored till date; however, following Bouillin and Kornprobst (1974), we conclude that the Yaddene complex is best explained as a sill emplaced within the fine-grained sediments constituting the upper part of the OMK during an extensional regime. We also note that silexites have been identified in the upper part of the OMK series (Géry et al., 1981) and attributed to the Upper Aquitanian/Middle Burdigalian. In Greater Kabylia, a rhyolitic tuff associated with a similar level of silexites has been dated by the K-Ar method at 19.1 ± 1.0 Ma (Bellon, 1976), which is consistent with the lower Burdigalian U-Pb zircon ages (18.97 ± 0.12 Ma and 19.05 ± 0.39 Ma) of the studied rocks. Thus, we argue that emplacement and crystallization of the Yaddene complex was synchronous to the syn-rift sedimentation that formed the OMK series.

Medaouri et al. (2014) identified a major extensional regime in the western part of the Algerian basin that started in the Burdigalian and affected the stretched continental crust of the Alboran to Algerian Basin transition zone. Furthermore, exhumation of basement rocks as a metamorphic core complex (Caby et al., 2001) in the Edough Massif occurred at *c.* 18 Ma (Bruguier et al., 2009). Thus, emplacement of the mafic and ultramafic rocks of the Yaddene complex occurred during a major and widespread phase of Burdigalian extensional tectonics that affected the western Mediterranean (Leprêtre et al., 2018) and ultimately led to the opening of the Algerian Basin. Major and trace element analyses of clinopyroxenes from the mafic and ultramafic rocks of the Yaddene complex (Figs. 6 and 11) provide geochemical signatures (LREE-depleted patterns, LILE enrichments, and HFSE negative anomalies) consistent with a back-arc basin environment, proximal to the arc. Thus, we propose that the Yaddene complex was emplaced at *c.* 19 Ma at low pressures (i.e., 1–3 kbars), corresponding to upper-crustal depths (≤12 km), in a back-arc environment that was associated with the southeastward retreat of the Tethyan slab. Slab rollback during this period was responsible for the extension of the Kabylian/North African margin and the development of a back-arc basin. It is difficult to determine the initiation of opening of the Algerian basin; however, the early Burdigalian age of the Yaddene complex is regarded as the minimum age for rift-related extensional tectonics. Further east, in the Edough area, thrusting of ultra-high-pressure oceanic units onto the margin of North Africa occurred at *c.* 21 Ma during the Aquitanian (Bosch et al., 2014; Caby et al., 2014; Fernandez et al., 2016; Bruguier et al., 2017), which further constrains the onset of extensional tectonics affecting the African margin at 19–21 Ma.

The *c.* 19 Ma age of the Yaddene complex has another indirect consequence. The onshore occurrence of the OMK series onto the stretched Kabylian basement and offshore filling of troughs in this basement implies that the Kabylies-Africa collision occurred before 19

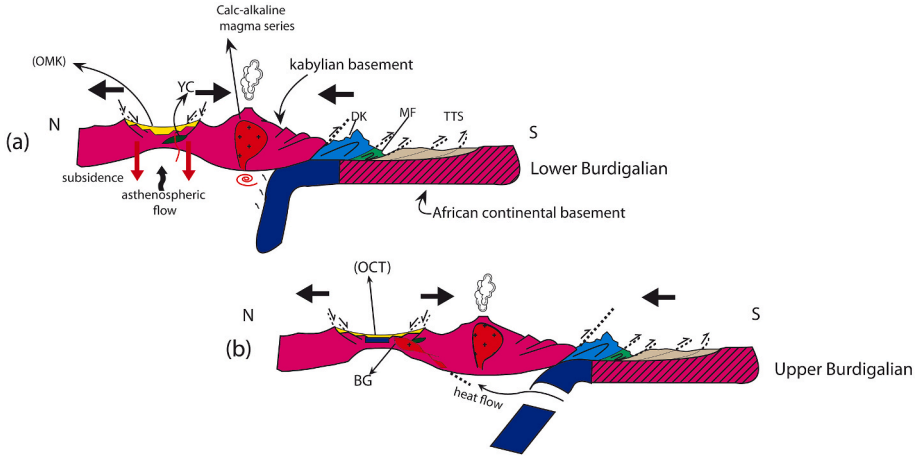

Fig. 14. Simplified explanatory sketch of the geodynamic evolution of the northeastern part of Algeria (Lesser Kabylia) during the lower Miocene. (a) opening of the Algerian basin as a back arc basin. Extensional tectonics related to slab roll-back was responsible for rifting of the Kabylian basement and deposition of the syn-rift "Oligo-Miocene Kabyle" series since the Upper Oligocene. Calc-alkaline granitoids, such as the Beni Toufout granite dated at 22–23 Ma (Bellon, 1976; Abbassene et al., 2016), were emplaced during this period onward. Thinning of the crust was accompanied by gabbroic intrusions in the extended crust such as the Yaddene complex dated at 19 Ma (this study); (b) Back-arc extension continued and may have been enhanced by slab break-off of the Tethyan slab at ca. 17 Ma (intrusion age of the Cap Bougaroun batolith; Abbassene et al., 2016) leading to fast oceanisation of the nascent Algerian basin. BG: Cap Bougaroun granite; DK: "Dorsale Kabyle"; OC: Oceanic crust; MF: Maghrebide flyschs; TTS: Tellian thrust sheets; YC: Yaddene Complex; OMK: Oligo Miocene Kabyle sediments.

Ma, i.e., in the early Miocene/Oligocene. This contrasts with the *c.* 16–18 Ma age, which is commonly reported for accretion of the Kabylies to the northern margin of Africa in most geodynamic reconstructions (Frizon de Lamotte et al., 2000; Handy et al., 2010; Leprêtre et al., 2018; van Hinsbergen et al., 2020). Thus, we suggest reconsidering the age of collision of the Kabylies earlier to the early Burdigalian and preferentially Aquitanian (c. 21 Ma). This is in agreement with the proposal of Romagny et al. (2020), who suggested docking of AlKaPeCa fragments along the northern margin of Africa at c. 20 Ma.

We proposed a reconstruction of the major events that occurred during the lower Miocene along the northern margin of Africa and were related to the opening of the Algerian Basin (Fig. 14). From c. 21 Ma onward, the North African margin and docked basement of the Kabylies underwent extensional tectonics that formed tilted blocks and deposited the syn-rift sediments (e.g., Arab et al., 2016). Mantle melting by adiabatic decompression produced tholeiitic melts with a back-arc geochemical signature. Some of these melts reached the upper crustal levels and formed magmatic complexes, such as the Yaddene complex, which crystallized at low pressures (1–3 kbar) at *c.* 19 Ma. Simultaneously, the lower crust was dragged out and exhumed as a metamorphic core complex further east in the Edough area at *c.* 18 Ma (Caby et al., 2001). This sequence of events is similar to that described for the Gulf of Lion (France), where extensional tectonics related to slab roll-back resulted in an extended upper crustal section with tilted geometries and the lower crust exhumed as metamorphic core complexes (e.g., Jolivet et al., 2015). These two sides of the Western Mediterranean (Gulf of Lion/Liguro Provençal basin and the North African margin/Algerian basin) represent OCT zones that both started their evolution in subaerial conditions during rifting and subsequently evolved into deep oceanic basins. The main difference lies in the timing of the rifting and oceanic phases, which are older in the Liguro-Provençal Basin. In the latter, the rifting phase occurred during the Oligocene/Early Miocene (c. 35–23 Ma, Faccenna et al., 2001) with oceanization during *c.* 24–15 Ma (Gattacceca et al., 2007); however, in the Algerian Basin, the proposed rifting phase is younger and apparently shorter (*c.* 21–17 Ma) (Fig. 14a). Although this inference requires further substantiation, a shorter rifting phase for the Algerian Basin is consistent with slab tearing and break-off along the African margin (Fig. 14b) (Wortel and Spakman, 2000; Fichtner and Villaseñor, 2015), which would have accelerated extensional processes and development of subsequent seafloor spreading (16–8 Ma; Mauffret et al., 2004).

7. Conclusion

Petrography of the mafic and ultramafic rocks from the layered Yaddene Complex shows that they were derived from the differentiation of a picritic magma, for which, in addition to the mineralogical composition already described we report the presence of primary amphiboles (pargasite).

In situ geochemical analyses of constitutive minerals indicate that they crystallized at high temperatures (860–1260 °C for olivine, plagioclase, and pyroxenes) and low pressures (0.9–3.4 kbars). These conditions are consistent with emplacement into a thin crust, and geochemical analyses further support a back-arc environment proximal to the magmatic arc.

In situ U-Pb dating of zircon and titanite from a quartz-bearing gabbro and of zircon form a plagioclase-bearing lherzolite provide ages of 18.97 ± 0.12 and 19.05 ± 0.34 Ma (2σ), respectively, which constrains the syn-rift sedimentation of the "Oligo-Miocene Kabyle" and the rifting phase leading to opening of the Algerian Basin to the lower Burdigalian.

Declaration of competing interest

The authors declare that they have no known competing financial interests or personal relationships that could have appeared to influence the work reported in this paper.

Data availability

Data will be made available on request.

Acknowledgments

A. S wishes to thank the Center of Research in Astronomy, Astrophysics and Geophysics for short-period grants to travel to Montpellier – France. A.S and N.A are grateful to the Géosciences Montpellier laboratory for providing access to instrumental facilities during this research work.

References

Abbassene, F., Chazot, G., Bellon, H., Bruguier, O., Ouabadi, A., Maury, R.C., Déverchére, J., Bosch, D., Monie, P., 2016. A 17 Ma onset for the post-collisional K-rich calc-alkaline magmatism in the Maghrebides: evidence from Bougaroun (northeastern Algeria) and geodynamic implications. Tectonophysics 674, 114–134. https://doi.org/10.1016/j.tecto.2016.02.013.

Allan, J.F., Sack, R.O., Batiza, R., 1988. Cr-rich spinels as petrogenetic indicators; MORB-type lavas from the Lamont seamount chain, eastern Pacific. Am. Mineral. 73 (7–8), 741–753.

Arab, M., Rabineau, M., Déverchère, J., Bracene, R., Belhai, D., Roure, F., Marok, A., Bouyahiaoui, B., Granjeon, D., Andriessen, P., Sage, F., 2016. Tectonostratigraphic evolution of the eastern Algerian margin and basin from seismic data and onshore-offshore correlation. Mar. Petrol. Geol. 77, 1355–1375. https://doi.org/10.1016/j.marpetgeo.2016.08.021.

Arai, S., 1992. Chemistry of chromian spinel in volcanic rocks as a potential guide to magma chemistry. Mineral. Mag. 56 (383), 173–184. https://doi.org/10.1180/minmag.1992.056.383.04.

Beccaluva, L., Macciotta, G., Piccardo, G.B., Zeda, O., 1989a. Clinopyroxene composition of ophiolite basalts as petrogenetic indicator. Chem. Geol. 77, 165–182. https://doi.org/10.1016/0009-2541(89)90073-9.

Beccaluva, L., Macciotta, G., Piccardo, G.B., Zeda, O., 1989b. Clinopyroxene composition of ophiolite basalts as petrogenetic indicator. Chem. Geol. 77 (3–4), 165–182. https://doi.org/10.1016/0009-2541(89)90073-9.

Belayouni, H., Guerrera, F., Martín-Martín, M., Serrano, F., 2013. Paleogeographic and geodynamic Miocene evolution of the Tunisian Tell (Numidian and post-Numidian successions): bearing with the Maghrebian chain. Int. J. Earth Sci. 102 (3), 831–855. https://doi.org/10.1007/s00531-012-0824-x.

Bellon, H., 1976. Séries magmatiques néogènes et quaternaires du pourtour de la Méditérranée occidentale, comparées dans leur cadre géochronométrique. Implications géodynamiques. Doctoral dissertation, université Paris-Sud Orsay, p. 367.

Bonatti, E., Michael, P.J., 1989. Mantle peridotites from continental rifts to ocean basins to subduction zones. Earth Planet Sci. Lett. 91 (3–4), 297–311.

Bosch, D., Hammor, D., Mechati, M., Fernandez, L., Bruguier, O., Caby, R., Verdoux, P., 2014. Geochemical study (major, trace elements and Pb-Sr-Nd isotopes) of mantle material obducted onto the North African margin (Edough Massif, North Eastern Algeria): Tethys fragments or lost remnants of the Liguro-Provençal basin. Tectonophysics 626, 53–68.

Bouillin, J.P., 1977. Géologie alpine de la Petite Kabylie dans les régions de Collo et d'El Milia (Algérie). Doctoral dissertation, p. 472. Toulouse.

Bouillin, J.P., 1986. Le" bassin maghrebin"; une ancienne limite entre l'Europe et l'Afrique a l'ouest des Alpes. Bull. Soc. Geol. Fr. 2 (4), 547–558.

Bouillin, J.P., Kornprobst, J., 1974. Associations ultrabasiques de Petite Kabylie; peridotites de type alpin et complexe stratifie; comparaison avec les zones internes betico-rifaines. Bull. Soc. Geol. Fr. 7 (2), 183–194.

Bouillin, J.P., Durand-Delga, M., Gelard, J.P., Leikine, M., Raoult, J.F., Raymond, D., Tefiani, M., Vila, J.M., 1970. Définition d'un flysch massylien et d'un flysch maurétanien au sein des flyschs allochtones de l'Algérie. CR Acad. Sci. Paris 270, 2249–2252.

Bouyahiaoui, B., Sage, F., Abtout, A., Klingelhoefer, F., Yelles-Chaouche, K., Schnürle, P., Marok, A., Déverchère, J., Arab, M., Galve, A., Collot, J.Y., 2015. Crustal structure of the eastern Algerian continental margin and adjacent deep basin: implications for late Cenozoic geodynamic evolution of the western Mediterranean. Geophys. J. Int. 201 (3), 1912–1938. https://doi.org/10.1093/gji/ggv102.

Boynton, W.V., 1984. Cosmochemistry of the rare earth elements: meteorite studies. In: Developments in Geochemistry, 2. Elsevier, pp. 63–114. https://doi.org/10.1016/b978-0-444-42148-7.50008-3.

Brey, G.P., Köhler, T., 1990. Geothermobarometry in four-phase lherzolites II. New thermobarometers, and practical assessment of existing thermobarometers. J. Petrol. 31 (6), 1353–1378. https://doi.org/10.1093/petrology/31.6.1353.

Bruguier, O., Hammor, D., Bosch, D., Caby, R., 2009. Miocene incorporation of peridotite into the Hercynian basement of the Maghrebides (Edough massif, NE Algeria): implications for the geodynamic evolution of the Western Mediterranean. Chem. Geol. 261 (1–2), 172–184. https://doi.org/10.1016/j.chemgeo.2008.11.016.

Bruguier, O., Bosch, D., Caby, R., Vitale-Brovarone, A., Fernandez, L., Hammor, D., Laouar, R., Ouabadi, A., Abdallah, N., Mechati, M., 2017. Age of UHP metamorphism in the Western Mediterranean: insight from rutile and minute zircon inclusions in a diamond-bearing garnet megacryst (Edough Massif, NE Algeria). Earth Planet Sci. Lett. 474, 215–225. https://doi.org/10.1016/j.epsl.2017.06.043.

Cabanis, B., Lecolle, M., 1989. Le diagramme La/10-Y/15-Nb/8: un outil pour la discrimination des séries volcaniques et la mise en évidence des processus de mélange et/ou de contamination crustale. Comptes rendus de l'Académie des sciences. Série 2, Mécanique, Physique, Chimie.

Caby, R., Hammor, D., Delor, C., 2001. Metamorphic evolution, partial melting and Miocene exhumation of lower crust in the Edough metamorphic core complex, west Mediterranean orogen, eastern Algeria. Tectonophysics 342 (3–4), 239–273. https://doi.org/10.1016/S0040-1951(01)00166-4.

Caby, R., Bruguier, O., Fernandez, L., Hammor, D., Bosch, D., Mechati, M., Laouar, R., Ouabadi, A., Abdallah, N., Douchet, C., 2014. Metamorphic diamonds in a garnet megacryst from the Edough Massif (northeastern Algeria). Recognition and geodynamic consequences. Tectonophysics 637, 341–353. https://doi.org/10.1016/j.tecto.2014.10.017.

De la Roche, H.D., Leterrier, J.T., Grandclaude, P., Marchal, M., 1980. A classification of volcanic and plutonic rocks using R1R2-diagram and major-element analyses—its relationships with current nomenclature. Chem. Geol. 29 (1–4), 183–210. https://doi.org/10.1016/0009-2541(80)90020-0.

Dick, H.J., Bullen, T., 1984. Chromian spinel as a petrogenetic indicator in abyssal and alpine-type peridotites and spatially associated lavas. Contrib. Mineral. Petrol. 86 (1), 54–76. https://doi.org/10.1007/BF00373711.

Duggen, S., Hoernle, K., van den Bogaard, P., Garbe-Schönberg, D., 2005. Post-collisional transition from subduction-to intraplate-type magmatism in the westernmost Mediterranean: evidence for continental-edge delamination of subcontinental lithosphere. J. Petrol. 46 (6), 1155–1201. https://doi.org/10.1093/petrology/egi013.

Durand-Delga, M., 1969. Mise au point sur la structure du Nord-Est de la Berbérie. Publ. Serv. Carte géol. Algérie, NS. Bull. Soc. Geol. Fr. 13 (7), 328–337.

Durand-Delga, M., 1980. Le cadre structural de la Méditerranée occidentale. Georogie des chaines alpines issues de la Tethys 67–85.

Faccenna, C., Becker, T.W., Lucente, F.P., Jolivet, L., Rossetti, F., 2001. History of subduction and back arc extension in the Central Mediterranean. Geophys. J. Int. 145 (3), 809–820. https://doi.org/10.1046/j.0956-540X.2001.01435.x.

Fernandez, L., Bosch, D., Bruguier, O., Hammor, D., Caby, R., Monié, P., Arnaud, N., Toubal, A., Galland, B., Douchet, C., 2016. Permo-Carboniferous and early Miocene geological evolution of the internal zones of the Maghrebides–New insights on the western Mediterranean evolution. J. Geodyn. 96, 146–173. https://doi.org/10.1016/j.jog.2015.10.001.

Fichtner, A., Villaseñor, A., 2015. Crust and upper mantle of the western Mediterranean–Constraints from full-waveform inversion. Earth Planet Sci. Lett. 428, 52–62. https://doi.org/10.1016/j.epsl.2015.07.038.

Frizon de Lamotte, D., Saint Bezar, B., Bracène, R., Mercier, E., 2000. The two main steps of the Atlas building and geodynamics of the western Mediterranean. Tectonics 19 (4), 740–761. https://doi.org/10.1029/2000TC900003, 000.

Gattacceca, J., Deino, A., Rizzo, R., Jones, D.S., Henry, B., Beaudoin, B., Vadeboin, F., 2007. Miocene rotation of Sardinia: new paleomagnetic and geochronological constraints and geodynamic implications. Earth Planet Sci. Lett. 258 (3–4), 359–377. https://doi.org/10.1016/j.epsl.2007.02.003.

Gee, L.L., Sack, R.O., 1988. Experimental petrology of melilite nephelinites. J. Petrol. 29 (6), 1233–1255.

Gelard, J.P., 1969. Le flysch à base schisto-gréseuse de la bordure méridionale et orientale du massif de Chellata; le flysch mauretanien (Grande-Kabylie, Algerie). Bull. Soc. Geol. Fr. 7 (5), 676–686.

Géry, B., Feinberg, H., Lorenz, C., Magné, J., 1981. Definition d'une série-type de l'Oligo-Miocene Kabyle anté-nappes dans le Djebel Aissa-Mimoun (Grande Kabylie, Algérie). *C. R. Acad. Sci.* Paris 292, 1529–1532.

Green, A.R., DeBari, S.M., Kelemen, P.B., Blusztajn, J., Clift, P.D., 2006. A detailed geochemical study of island Arc crust: The Talkeetna Arc section, south-central Alaska. J. Petrol. 1051–1093. https://doi.org/10.1093/petrology/egl002.

Günther, D., Heinrich, C.A., 1999. Enhanced sensitivity in laser ablation-ICP mass spectrometry using helium-argon mixtures as aerosol carrier. J. Anal. At. Spectrom. 14 (9), 1363–1368. https://doi.org/10.1039/a901648a.

Hammor, D., Bosch, D., Caby, R., Bruguier, O., 2006. A two-stage exhumation of the Variscan crust: U–Pb LA-ICP-MS and Rb–Sr ages from Greater Kabylia, Maghrebides. Terra. Nova 18 (5), 299–307. https://doi.org/10.1111/j.1365-3121.2006.00693.x.

Handy, M.R., Schmid, S.M., Bousquet, R., Kissling, E., Bernoulli, D., 2010. Reconciling plate-tectonic reconstructions of Alpine Tethys with the geological–geophysical record of spreading and subduction in the Alps. Earth Sci. Rev. 102 (3–4), 121–158. https://doi.org/10.1016/j.earscirev.2010.06.002.

Hawthorne, F.C., Oberti, R., Harlow, G.E., Maresch, W.V., Martin, R.F., Schumacher, J. C., Welch, M.D., 2012. Nomenclature of the amphibole supergroup. Am. Mineral. 97 (11–12), 2031–2048. https://doi.org/10.2138/am.2012.4276.

Heaman, L.M., 2009. The application of U-Pb geochronology to mafic, ultramafic and alkaline rocks: an evaluation of three mineral standards. Chem. Geol. 261, 43–52.

Herzberg, C., O'hara, M.J., 1998. Phase equilibrium constraints on the origin of basalts, picrites, and komatiites. Earth Sci. Rev. 44 (1–2), 39–79.

Hirose, K., Kawamoto, T., 1995. Hydrous partial melting of lherzolite at 1 GPa: the effect of H2O on the genesis of basaltic magmas. Earth Planet Sci. Lett. 133 (3–4), 463–473. https://doi.org/10.1016/0012-821X(95)00096-U.

Jackson, S.E., Pearson, N.J., Griffin, W.L., Belousova, E.A., 2004. The application of laser ablation-inductively coupled plasma-mass spectrometry to in situ U–Pb zircon geochronology. Chem. Geol. 211 (1–2), 47–69. https://doi.org/10.1016/j.chemgeo.2004.06.017.

Jolivet, L., Gorini, C., Smit, J., Leroy, S., 2015. Continental breakup and the dynamics of rifting in back-arc basins: the Gulf of Lion margin. Tectonics 34, 662–679. https://doi.org/10.1002/2014TC003570.

Kamenetsky, V.S., Crawford, A.J., Eggins, S., Mühe, R., 1997. Phenocryst and melt inclusion chemistry of near-axis seamounts, Valu Fa Ridge, Lau Basin: insight into mantle wedge melting and the addition of subduction components. Earth Planet Sci. Lett. 151 (3–4), 205–223. https://doi.org/10.1016/s0012-821x(97)81849-3.

Kamenetsky, V.S., Crawford, A.J., Meffre, S., 2001. Factors controlling chemistry of magmatic spinel: an empirical study of associated olivine, Cr-spinel and melt inclusions from primitive rocks. J. Petrol. 42 (4), 655–671. https://doi.org/10.1093/petrology/42.4.655, 42, 655–671.

Le Bas, M.J., 1962. The role of aluminum in igneous clinopyroxenes with relation to their parentage. Am. J. Sci. 260 (4), 267–288. https://doi.org/10.2475/ajs.260.4.267.

Leprêtre, R., Frizon de Lamotte, D., Combier, V., Gimeno-Vives, O., Mohn, G., Eschard, R., 2018. The Tell-Rif orogenic system (Morocco, Algeria, Tunisia) and the structural heritage of the southern Tethys margin. BSGF-Earth Sciences Bulletin 189 (2), 10. https://doi.org/10.1051/bsgf/2018009.

Leterrier, J., Maury, R.C., Thonon, P., Girard, D., Marchal, M., 1982. Clinopyroxene composition as a method of identification of the magmatic affinities of paleo-volcanic series. Earth Planet Sci. Lett. 59 (1), 139–154. https://doi.org/10.1016/0012-821X(82)90122-4.

Li, J.P., 1991. *Evolution chimique des phases solides dans la fusion partielle et la rééquilibration de subsolidus des péridotites naturelles: étude expérimentale et applications* (Doctoral dissertation).

Ludwig, K.R., 2003. Mathematical-statistical treatment of data and errors for 230Th/U geochronology. Uranium-series Geochemistry 52, 631–656. https://doi.org/10.1515/9781501509308-021.

Ludwig, K.R., 2003. Mathematical–statistical treatment of data and errors for 230Th/U geochronology. Rev. Mineral. Geochem. 52 (1), 631–656. https://doi.org/10.1515/9781501509308-021.
Mahdjoub, Y., 1991. Cinématique des déformations et évolution P-. T anté-alpines en Petite Kabylie (Algérie Nord Orientale). Doctoral dissertation, Thèse Doctorat d'Etat, p. 194. USTHB, Alger.
Mahdjoub, Y., Merle, O., 1990. Cinématique des déformations tertiaires dans le massif de Petite Kabylie (Algérie orientale). Bull. Soc. Geol. Fr. 6 (4), 629–634.
Mahdjoub, Y., Choukroune, P., Kienast, J.R., 1997. Kinematics of a complex Alpine segment; superimposed tectonic and metamorphic events in the Petite Kabylie Massif (northern Algeria). Bull. Soc. Geol. Fr. 168 (5), 649–661.
Marocchi, M., Mair, V., Tropper, P., Bargossi, G.M., 2009. Metasomatic reaction bands at the Mt. Hochwart gneiss-peridotite contact (Ulten Zone, Italy): insights into fluid-rock interaction in subduction zones. Mineral. Petrol. 95, 251–272.
Mauffret, A., Frizon de Lamotte, D., Lallemant, S., Gorini, C., Maillard, A., 2004. E–W opening of the Algerian Basin (western Mediterranean). Terra. Nova 16 (5), 257–264. https://doi.org/10.1111/j.1365-3121.2004.00559.x.
Medaouri, M., Déverchère, J., Graindorge, D., Bracene, R., Badji, R., Ouabadi, A., Yelles-Chaouche, K., Bendiab, F., 2014. The transition from Alboran to Algerian basins (Western Mediterranean Sea): chronostratigraphy, deep crustal structure and tectonic evolution at the rear of a narrow slab rollback system. J. Geodyn. 77, 186–205. https://doi.org/10.1016/j.jog.2014.01.003.
Michard, A., Negro, F., Saddiqi, O., Bouybaouene, M.L., Chalouan, A., Montigny, R., Goffé, B., 2006. Pressure–temperature–time constraints on the Maghrebide mountain building: evidence from the Rif–Betic transect (Morocco, Spain), Algerian correlations, and geodynamic implications. Compt. Rendus Geosci. 338 (1–2), 92–114. https://doi.org/10.1016/j.crte.2005.11.011.
Middlemost, E.A., 1986. Magmas and Magmatic Rocks: an Introduction to Igneous Petrology.
Morimoto, N., 1988. Nomenclature of pyroxenes. Mineral. Petrol. 39 (1), 55–76. https://doi.org/10.1007/BF01226262.
Otten, M.T., 1984. The origin of brown hornblende in the Artfjället gabbro and dolerites. Contrib. Mineral. Petrol. 86 (2), 189–199.
Ouabadi, A., 1994. Pétrologie, géochimie et origine des granitoïdes peralumineux à cordiérite (Cap Bougaroun, Beni-Touffout et Filfila) Algérie nord-orientale. Doctoral dissertation, p. 232. Rennes 1.
Palme, H., O'Neill, H.S., 2003. Cosmochemical estimates of mantle composition. In: Holland, H.D., Turekian, K.K. (Eds.), Treatise on Geochemistry, 2. Elsevier, pp. 1–38.
Pearce, J.A., 1982. Trace element characteristics of lavas from destructive plate boundaries. Orogenic andesites and related rocks 528–548.
Pearce, J.A., 2008. Geochemical fingerprinting of oceanic basalts with applications to ophiolite classification and the search for Archean oceanic crust. Lithos 100 (1–4), 14–48. https://doi.org/10.1016/j.lithos.2007.06.016.
Pearce, J.A., 2014. Immobile element fingerprinting of ophiolites. Elements 10 (2), 101–108. https://doi.org/10.2113/gselements.10.2.101.
Pearce, J.A., Norry, M.J., 1979. Petrogenetic implications of Ti, Zr, Y, and Nb variations in volcanic rocks. Contrib. Mineral. Petrol. 69 (1), 33–47. https://doi.org/10.1007/BF00375192.
Pearce, N.J., Perkins, W.T., Westgate, J.A., Gorton, M.P., Jackson, S.E., Neal, C.R., Chenery, S.P., 1997. A compilation of new and published major and trace element data for NIST SRM 610 and NIST SRM 612 glass reference materials. Geostand. Newsl. 21 (1), 115–144.
Pearce, J.A., Stern, R.J., Bloomer, S.H., Fryer, P., 2005. Geochemical mapping of the Mariana arc-basin system: implications for the nature and distribution of subduction components. G-cubed 6 (7). https://doi.org/10.1029/2004GC000895.
Peccerillo, A., Taylor, S.R., 1976. Geochemistry of Eocene calc-alkaline volcanic rocks from the Kastamonu area, northern Turkey. Contrib. Mineral. Petrol. 58 (1), 63–81. https://doi.org/10.1007/BF00384745.
Perfit, M.R., Gust, D.A., Bence, A.E., Arculus, R.J., Taylor, S.R., 1980. Chemical characteristics of island-arc basalts: implications for mantle sources. Chem. Geol. 30 (3), 227–256. https://doi.org/10.1016/0009-2541(80)90107-2.
Peucat, J.J., Mahdjoub, Y., Drareni, A., 1996. U/Pb and Rb/Sr geochronological evidence for late Hercynian tectonic and Alpine overthrusting in Kabylian metamorphic basement massifs (northeastern Algeria). Tectonophysics 258 (1–4), 195–213. https://doi.org/10.1016/0040-1951(95)00197-2.
Putirka, K.D., 2005. Igneous thermometers and barometers based on plagioclase+ liquid equilibria: tests of some existing models and new calibrations. Am. Mineral. 90 (2–3), 336–346. https://doi.org/10.2138/am.2005.1449.
Putirka, K.D., 2008. Thermometers and barometers for volcanic systems. Rev. Mineral. Geochem. 69 (1), 61–120. https://doi.org/10.2138/rmg.2008.69.3.
Putirka, K.D., Perfit, M., Ryerson, F.J., Jackson, M.G., 2007. Ambient and excess mantle temperatures, olivine thermometry, and active vs. passive upwelling. Chem. Geol. 241 (3–4), 177–206. https://doi.org/10.1016/j.chemgeo.2007.01.014.
Raoult, J.F., 1969. La série de Tengout: unité externe de la dorsale Kabyle annonçant le Flysch de Penthièvre (Nord du Constantinois, Algérie). Bull. Serv. Géol. Fr 7.
Roda, M., Regorda, A., Spalla, M.I., Marotta, A.M., 2019. What drives A lpine T ethys opening? Clues from the review of geological data and model predictions. Geol. J. 54 (4), 2646–2664. https://doi.org/10.1002/gj.3316.
Roeder, P.L., Emslie, R., 1970. Olivine-liquid equilibrium. Contrib. Mineral. Petrol. 29 (4), 275–289.
Romagny, A., Jolivet, L., Menant, A., Bessiere, E., Maillard, A., Canva, A., Gorini, C., Augier, R., 2020. Detailed tectonic reconstructions of the Western Mediterranean region for the last 35 Ma, insights on driving mechanisms. BSGF - Earth Sci. Bull. 191, 37.
Ross, P.S., Bédard, J.H., 2009. Magmatic affinity of modern and ancient subalkaline volcanic rocks determined from trace-element discriminant diagrams. Can. J. Earth Sci. 46 (11), 823–839. https://doi.org/10.1139/E09-054.
Scowen, P.A.H., Roeder, P.L., Helz, R.T., 1991. Reequilibration of chromite within Kilauea Iki lava lake, Hawaii. Contrib. Mineral. Petrol. 107 (1), 8–20.
Shervais, J.W., 1982. Ti-V plots and the petrogenesis of modern and ophiolitic lavas. Earth Planet Sci. Lett. 59 (1), 101–118. https://doi.org/10.1016/0012-821X(82)90120-0.
Sisson, T.W., Grove, T.L., 1993a. Experimental investigations of the role of H_2O in calc-alkaline differentiation and subduction zone magmatism. Contrib. Mineral. Petrol. 113 (2), 143–166. https://doi.org/10.1007/BF00283225.
Sisson, T.W., Grove, T.L., 1993b. Temperatures and H_2O contents of low-MgO high-alumina basalts. Contrib. Mineral. Petrol. 113 (2), 167–184. https://doi.org/10.1007/BF00283226.
Spandler, C., Hammerli, J., Sha, P., Hilbert-Wolf, H., Hu, Y., Roberts, E., Schmitz, M., 2016. MKED1: a new titanite standard for in-situ analysis of Sm-Ndisotopes and U-Pb geochronology. Chem. Geol. 425, 110–126.
Speranza, F., Villa, I.M., Sagnotti, L., Florindo, F., Cosentino, D., Cipollari, P., Mattei, M., 2002. Age of the Corsica–Sardinia rotation and Liguro–Provençal basin spreading: new paleomagnetic and Ar/Ar evidence. Tectonophysics 347 (4), 231–251. https://doi.org/10.1016/S0040-1951(02)00031-8.
Stern, R.J., Ali, K., Asimow, P.D., Azer, M.K., Leybourne, M.I., Mubarak, H.S., Ren, M., Romer, R.L., Whitehouse, M.J., 2020. The Atud gabbro-diorite complex: glimpse of the Cryogenian mixing, assimilation, storage and homogenization zone beneath the Eastern Desert of Egypt. J. Geol. Soc. London 177, 965–980. https://doi.org/10.1144/jgs2019-199.
Sun, S.S., McDonough, W.F., 1989. Chemical and isotopic systematics of oceanic basalts: implications for mantle composition and processes. Geological Society, London, Special Publications 42 (1), 313–345. https://doi.org/10.1144/GSL.SP.1989.042.01.19.
Takahashi, E., 1985. Origin of basaltic magma-Implications from peridotite melting experiments and an olivine fractionation model. Bull. Volcanol. Soc. Jpn. 30, S17–S40.
Tribuzio, R., Tiepolo, M., Fiameni, S., 2008. A mafic-ultramafic cumulate sequence derived from boninite-type melts (Niagara Icefalls, northern Victoria Land, Antarctica). Contrib. Mineral. Petrol. 155 (5), 619–633. https://doi.org/10.1007/s00410-007-0261-1.
Tumiati, S., Godard, G., Martin, S., Klotzli, U., Monticelli, D., 2007. Fluid-controlled crustal metasomatism within a high-pressure subducted mélange (Mt Hochwart, Eastern Italian Alps). Lithos 94, 148–167.
Van Actherbergh, E., 2001. Data Reduction Software for LA-ICP-MS. Laser Ablation-ICP-Mass Spectrometry in the Earth Sciences: Principles and Applications, pp. 239–243.
Van Hinsbergen, D.J.J., Snel, E., Garstman, S.A., Mărunţeanu, M., Langereis, C.G., Wortel, M.J.R., Meulenkamp, J.E., 2004. Vertical motions in the Aegean volcanic arc: evidence for rapid subsidence preceding volcanic activity on Milos and Aegina. Mar. Geol. 209 (1–4), 329–345.
Van Hinsbergen, D.J., Torsvik, T.H., Schmid, S.M., Maţenco, L.C., Maffione, M., Vissers, R.L., Gürer, D., Spakman, W., 2020. Orogenic architecture of the Mediterranean region and kinematic reconstruction of its tectonic evolution since the Triassic. Gondwana Res. 81, 79–229. https://doi.org/10.1016/j.gr.2019.07.009.
Wells, P.R., 1977. Pyroxene thermometry in simple and complex systems. Contrib. Mineral. Petrol. 62 (2), 129–139. https://doi.org/10.1007/BF00372872.
Wiedenbeck, M.A.P.C., Alle, P., Corfu, F.Y., Griffin, W.L., Meier, M., Oberli, F.V., Von Quadt, A., Roddick, J.C., Spiegel, W., 1995. Three natural zircon standards for U-Th-Pb, Lu-Hf, trace element and REE analyses. Geostand. Newsl. 19 (1), 1–23.
Wildi, W., 1983. La chaîne tello-rifaine (Algérie, Maroc, Tunisie): structure, stratigraphie et évolution du Trias au Miocène. Rev. Geogr. Phys. Geol. Dyn. 24 (3), 201–297.
Wortel, M.J.R., Spakman, W., 2000. Subduction and slab detachment in the Mediterranean-Carpathian region. Science 290 (5498), 1910–1917. https://doi.org/10.1126/science.290.5498.1910.